Scientific Reports

https://doi.org/10.1038/s41598-026-57008-0

Article in Press

Experimental and numerical simulation assessment of fracture evolution and tensile strength recovery in Grout-reinforced fractured surrounding rocks

Received: 3 April 2026

Accepted: 4 June 2026

Published online: 11 June 2026

Cite this article as: Kolawole O., Sonibare M.O. & Olorode O. Experimental and numerical simulation assessment of fracture evolution and tensile strength recovery in Grout-reinforced fractured surrounding rocks. *Sci Rep* (2026). https://doi.org/10.1038/s41598-026-57008-0

Oladoyin Kolawole, Matthew O. Sonibare & Olufemi Olorode

Experimental and Numerical Simulation Assessment of Fracture Evolution and Tensile Strength Recovery in Grout-Reinforced Fractured Surrounding Rocks

Oladoyin Kolawole[a,*], Matthew O. Sonibare[a], Olufemi Olorode[b]

[a]*Department of Civil and Environmental Engineering, New Jersey Institute of Technology, Newark, NJ 07102, USA*

[b]*Department of Petroleum Engineering, Louisiana State University, Baton Rouge, LA 70803, USA*

[*]Corresponding author: oladoyin.kolawole@njit.edu

Abstract

The surrounding rock around deep underground excavations generally contains fractures and joints that significantly reduce mechanical integrity, particularly in zones where excavation-induced unloading, stress rotation, and anisotropic deformation generate tensile stress concentrations. These tensile regimes govern crack initiation, fracture propagation, spalling, and progressive instability around tunnels, caverns, mines, and wellbores. Although grouting is widely used as a reinforcement strategy, its effectiveness in restoring the inherent strength of tension-dominated surrounding rock is often assumed, and the tensile fracture behavior of fracture-grouted rock remains insufficiently understood. This study investigated the evolution of tensile strength (*TS*) and tensile-induced fracture behavior in fractured surrounding rock before and after fracture grouting, providing mechanistic evidence for assessing strength recovery. In addition to *TS*, failure modes and total fracture length (*TFL*) were quantified to assess fracture propagation and grout-reinforcement performance in tension-prone surrounding rock zones. Brazilian disc tests (BDT) were conducted on natural (limestone and dolomite) and synthetic (3D-printed) rock samples, allowing direct comparison of the same samples in ungrouted and fracture-grouted states. To mechanistically interpret and validate the experimental findings, a finite element model employing the cohesive zone method (FEM-CZM) implemented in ABAQUS was developed to simulate the evolution of tensile strength and the initiation and propagation of micro-fracture in the specimens before and after grouting. Results revealed that while fracture grouting does not fully restore the inherent tensile strength of fractured rocks, it significantly altered the tensile failure process. Grout–rock interfaces in the fracture-grouted rocks constrained and redirected crack propagation, reduced total fracture length, and shifted failure modes toward more localized and controlled fracture patterns. A positively correlated *TS*–*TFL* relationship observed in ungrouted samples reversed in fracture-grouted samples, indicating that higher tensile resistance in grouted rock mass corresponds to more limited fracture development. The FEM-CZM simulation confirmed the experimentally observed post-grouting delay in rock damage onset with reduced fracture path and an increase in Mode-II energy dissipation, and provided direct visualization of stress concentration, damage evolution, and fracture-path control. These findings demonstrate that surrounding rock control in tensile regimes depends not only on tensile strength recovery but also on the ability of grouting to suppress fracture propagation and damage evolution. The results provide new mechanistic insight into fracture-grouting performance in tension-prone underground environments and demonstrate that *TFL*, when used alongside tensile strength and other mechanical parameters, is a valuable metric for assessing reinforcement effectiveness. This work advances the understanding of grouting as a surrounding rock control strategy and informs the design of reinforcement systems aimed at stabilizing underground excavations subjected to tensile stress concentrations.

Keywords: Tensile strength; Surrounding rock control; Fracture grouting; Underground excavation; FEM-CZM; Brazilian disc test; Numerical simulation; Rock mass reinforcement; Grout–rock interface; Total fracture length

1 Introduction

Surrounding rock forms the immediate geological media around underground excavations like tunnels, caverns, wellbore, and mines; and its stability governs the safety and performance of underground structures and is strongly influenced by the mechanical behavior of the rock mass and its embedded discontinuities (such as fractures, joints, bedding planes, and faults) which serve as the foundation or host medium for various underground engineering structures constructed on or within them (Terzaghi, 1946; Barton et al., 1974; Bieniawski, 1973, 1993; Hoek, 1994; Cook et al., 1996; Hudson et al., 2002; Goel & Singh, 2011; Bell, 2013; Alejano, 2024). In deep or complex geological settings, the surrounding rocks are routinely subjected to high in-situ stresses, excavation-induced and anisotropic deformations, and stress rotation, all of which can trigger tensile stress concentrations around excavation perimeters which causes development of weakness planes in the rocks and can promote crack initiation, extension, and coalescence along pre-existing fractures, bedding planes, and joints (Haeri et al., 2014; Li et al., 2017; Askaripour et al., 2022; Bi et al., 2025), thereby compromising the load-bearing capacity and integrity of the surrounding rocks (Carter et al., 1992; Diederichs & Kaiser, 1999; Martino & Chandler, 2004; Cai, 2007; Alcalde-Gonzalo et al., 2013; Cai & Kaiser, 2013; Lei et al., 2017; Chen et al., 2020; Jiang et al., 2020). Rock masses in the underground environment are inherently discontinuous systems, and their behavior is dominated by the presence, geometry, and evolution of natural defects such as fractures, joints, and weak planes (Liao et al., 1997; Diederichs & Kaiser, 1999; Shen et al., 2018; Heidarzadeh et al., 2019; Chen et al., 2020; Askaripour et al., 2022; Cai et al., 2023; Hou et al., 2023; Úcar et al., 2023; Wen et al., 2023; Bi et al., 2025; Li et al., 2025).

Tensile failure, although less frequently studied than compressive or shear failure, plays a critical role in controlling surrounding rock deformation and instability in underground environment because even minimal tensile stresses can initiate brittle fracture, roof spalling, block detachment, and slabby failures that reduce effective confinement and enable progressive degradation of excavation boundaries (Baker, 1981; Carter et al., 1992; Diederichs & Kaiser, 1999; Alcalde-Gonzalo et al., 2013; Perras & Diederichs, 2014; Li et al., 2017; Shojaei & Shao, 2017; Tang et al., 2017; Bi et al., 2025; Li et al., 2025; Xu et al., 2025). In deep underground spaces, tensile-induced fractures and spalling can evolve and accelerate into large-scale structural instability, threatening long-term operational safety and increasing support demands (Diederichs & Kaiser, 1999; Alcalde-Gonzalo et al., 2013; Shojaei & Shao, 2017; Perras & Diederichs, 2014; Li et al., 2017; Tang et al., 2017; Liu et al., 2020; Askaripour et al., 2022; Úcar et al., 2023; Jing et al., 2023; Bi et al., 2025). The tensile failure around surrounding rocks is highly modulated by rock anisotropy (e.g., filled discontinuities), which redirects stress trajectories and steers fracture paths (Perras & Diederichs, 2014; Wang et al., 2022); therefore, the accurate characterization of tensile strength and tensile-induced failure mechanisms is essential to be studied for designing reinforcement strategies necessary for surrounding rock control. The Brazilian Disc Test (BDT) remains one of the most widely used methods for quantifying the splitting tensile strength (*TS*) of rock specimens and for capturing tensile fracture patterns under controlled loading (ISRM, 1978; ASTM, 2023). However, the influence of rock anisotropy, test loading alignment, and internal heterogeneity can cause substantial variation in observed tensile failure modes (Stacey, 1981; Markides & Kourkoulis, 2024), highlighting the need to analyze *TS* values together with rock fracture morphology and failure trajectories. In underground engineering practice, such measurements support excavation design, support selection, and risk assessments for spalling, tensile overstress, and other brittle failure processes (Jinpeng et al., 2023).

To enhance the integrity of fractured surrounding rock, grouting is commonly used as a reinforcement method to fill discontinuities, reduce permeability, stiffen fractured zones, and improve the composite response of the rock mass (Liu & Li, 2017; Sang et al., 2024; Oppong & Kolawole, 2025; Sonibare et al., 2025; Sonibare & Kolawole, 2025; Ngoma & Kolawole, 2026; Song et al., 2026); and its mechanisms include aperture reduction, asperity interlocking, and the creation of composite grout–rock bridges across defects (Salimian et al., 2017; Ma & Ma, 2021; Sang et al., 2024). While its benefits in improving compressive and shear strength are well-established (Hou et al., 2022; Wang et al., 2022; Oppong & Kolawole, 2025; Sonibare et al., 2025, 2026; Sonibare & Kolawole, 2025; Ngoma & Kolawole, 2026), the role of grouted fractures in modifying tensile behavior to yield structural anisotropy and the capacity of rock fracture grouting to control tensile fracture development in surrounding rock remains insufficiently understood, especially in tensile-dominated zones. However, this unsubstantiated assumption that grouting fully restores the natural strength and stability of surrounding rock masses is yet to be experimentally and numerically validated.

To mitigate rock mass failure and collapse of underground infrastructure, rock reinforcement schemes commonly combine grouting and rock bolts to increase stiffness, reduce permeability, and mobilize composite action across fractures and bedding (Liu & Li, 2017; Wen et al., 2025; Wang et al., 2025; Yuan et al., 2025). Grouted systems can enhance rock failure resistance via asperity interlocking and cementation, while bolting contributes to axial and shear capacity under mixed loading (Wu et al., 2003; Salimian et al., 2017). Extensive laboratory and field studies on fractured rocks generally report gains in compressive strength and shear failure resistance after grouting (Salimian et al., 2017; Liu et al., 2020; Ma & Ma, 2021). Further, grout type, grout rheology, and penetration depth influence these compressive properties and joint shear behavior in underground rock masses (Ma & Ma, 2021; Sang et al., 2024; Liu et al., 2020). Yet, whether and to what extent rock grouting improves tensile strength and tensile failure resistance of rock masses remains comparatively underexplored, even though tension-dominated regimes are common around excavation perimeters, in stratified or weathered rock masses, and where stress rotation concentrates extension (Diederichs & Kaiser, 1999; Perras & Diederichs, 2014). The grout–rock interface, residual micro-fractures, and spatially variable grout materials may either arrest fractures or introduce new weak planes, so compressive strength gains do not automatically translate into higher *TS* or to favorable fracture-propagation behavior (Salimian et al., 2017; Liu et al., 2020).

Complementing laboratory experiments, numerical simulation offers unique mechanistic insights into rock fracture initiation, propagation, and coalescence processes that are inaccessible or difficult to directly observe experimentally (Han et al., 2020a, 2020b; Du et al., 2021; Asadizadeh et al., 2025). The coupling of the finite element method (FEM) with the cohesive zone model (FEM-CZM) has been widely and successfully employed for simulating rock fracture behavior in disc specimens containing pre-existing cracks and interfaces in rock and rock-like materials (Du et al., 2021; Meng et al., 2021; Han et al., 2020b; Asadizadeh et al., 2025; Liu et al., 2025), and the commercial FE package ABAQUS provides a robust platform for CZM implementation (Navidtehrani et al., 2021; Han et al., 2020b). Despite progress in numerically simulating fracture behavior of rock discs, no prior study has implemented FEM-CZM to explicitly model and compare micro-fracture initiation and propagation in rock disc specimens across ungrouted fractured and fracture-grouted conditions.

Bridging these knowledge gaps is critical because surrounding rock control depends not only on restoring bulk rock tensile strength but also on managing localized fracture evolution due to excavation-induced stress rotation, differential deformation, blasting, thermal loads, or time-dependent deterioration. The length and intensity of fractures are key structural parameters influencing the tensile strength of rock masses (Khanlari et al., 2015, 2019; Abdi, 2024; Zhou et al., 2025; Bian et al., 2026). Khanlari et al. (2015)

suggested that total fracture length (*TFL*) could serve as an index parameter correlated with tensile strength, offering additional insight into fracture propagation processes and damage accumulation. However, the utility of such a metric for fracture-grouted systems has not been rigorously evaluated. Synthetic rock-like analogs (3D-printed rocks) allow decoupling of lithology from fracture geometry, supporting systematic tests on how grout changes tensile failure across prescribed defects (Perras & Diederichs, 2014; Jiang & Zhao, 2015; Hong et al., 2024), but their use in fracture-grouting studies remains limited.

To address these challenges, this study systematically investigates the evolution of tensile strength (*TS*) and tensile-induced crack behavior of fractured surrounding rock before and after fracture grouting for strength recovery assessment, and further quantifies the failure modes and total fracture length (*TFL*) to evaluate fracture propagation and grout reinforcement performance within tension-prone surrounding rock zones. Using Brazilian disc tests (BDT), natural (limestone and dolomite) and synthetic (3D-printed) rock samples are compared before and after fracture grouting, allowing direct baseline comparison of the same specimens in ungrouted and fracture-grouted states. A total of thirty-one (31) specimens were subjected to sixty-one (61) BDT tests before and after grouting with nanomagnetic slurry to quantify the degree of tensile strength restoration and evaluate changes in fracture morphology. A new FEM-CZM-based numerical simulation framework implemented in ABAQUS will be developed to mechanistically interpret and extend the experimental observations.

2 Method and Data

The summary of the experimental approach and analyses in this study is illustrated in Figure .

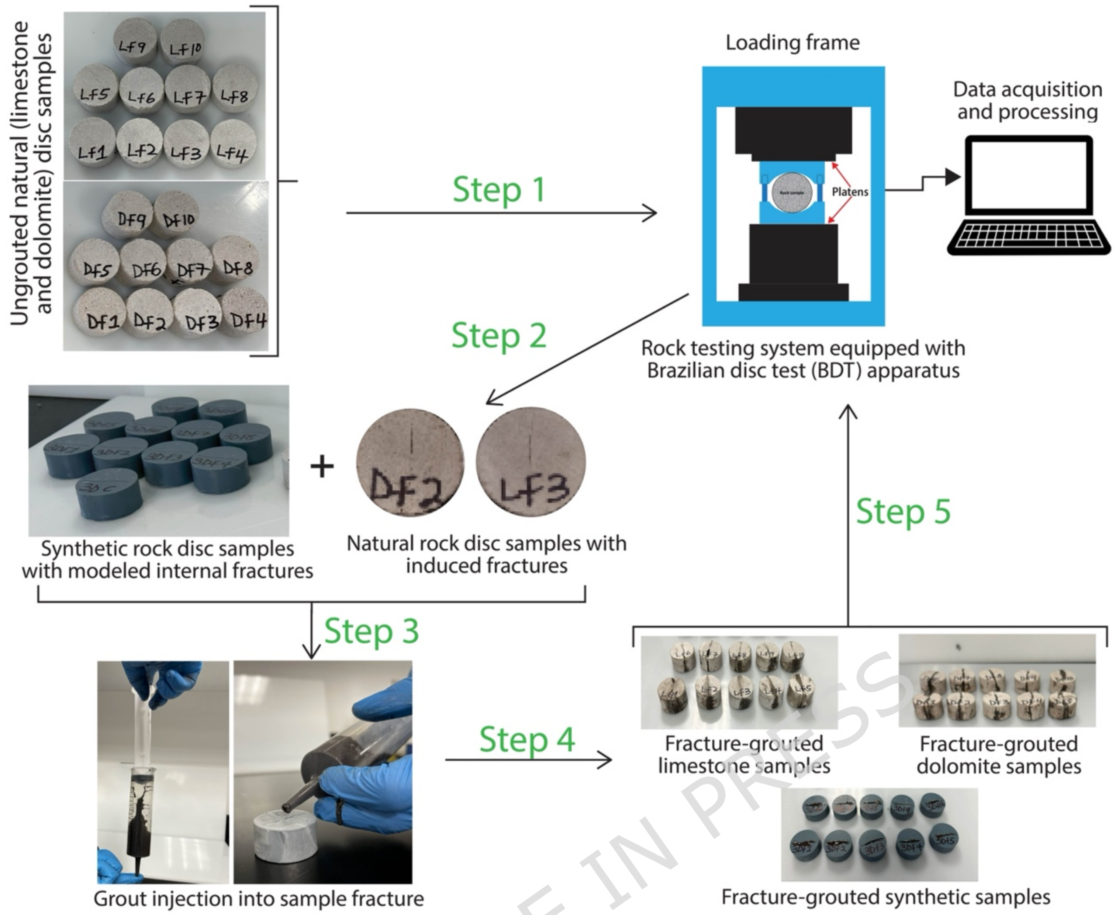

Figure 1: Experimental workflow used in this study.

2.1 Materials and Methods

2.1.1 Rock Disc Samples

In this study, thirty-one (31) rock samples (Fig. 2), comprising natural limestone and dolomite rock discs from deep underground strata within the USA and synthetic (3D-printed) analogs, were tested using the Brazilian disc test (BDT) across ungrouted and fracture-grouted conditions, as summarized in Table 1. The natural rock blocks were prepared into disc samples of 3.81 cm diameter and 1.91 cm thickness (Fig. 2a-b) according to the established rock mechanics standard for BDT (ISRM, 1978; ASTM, 2023). The natural rock disc surfaces were cut parallel and smoothened so that irregularities were less than 0.25 mm, with the two faces parallel to within 0.25° accuracy. To enable reliable comparisons based on anisotropy created by grouting of induced fractures, the natural rock samples contained no pre-existing natural fractures or stratification, allowing tensile stress to govern the orientation and direction of tensile-induced fractures in the specimens.

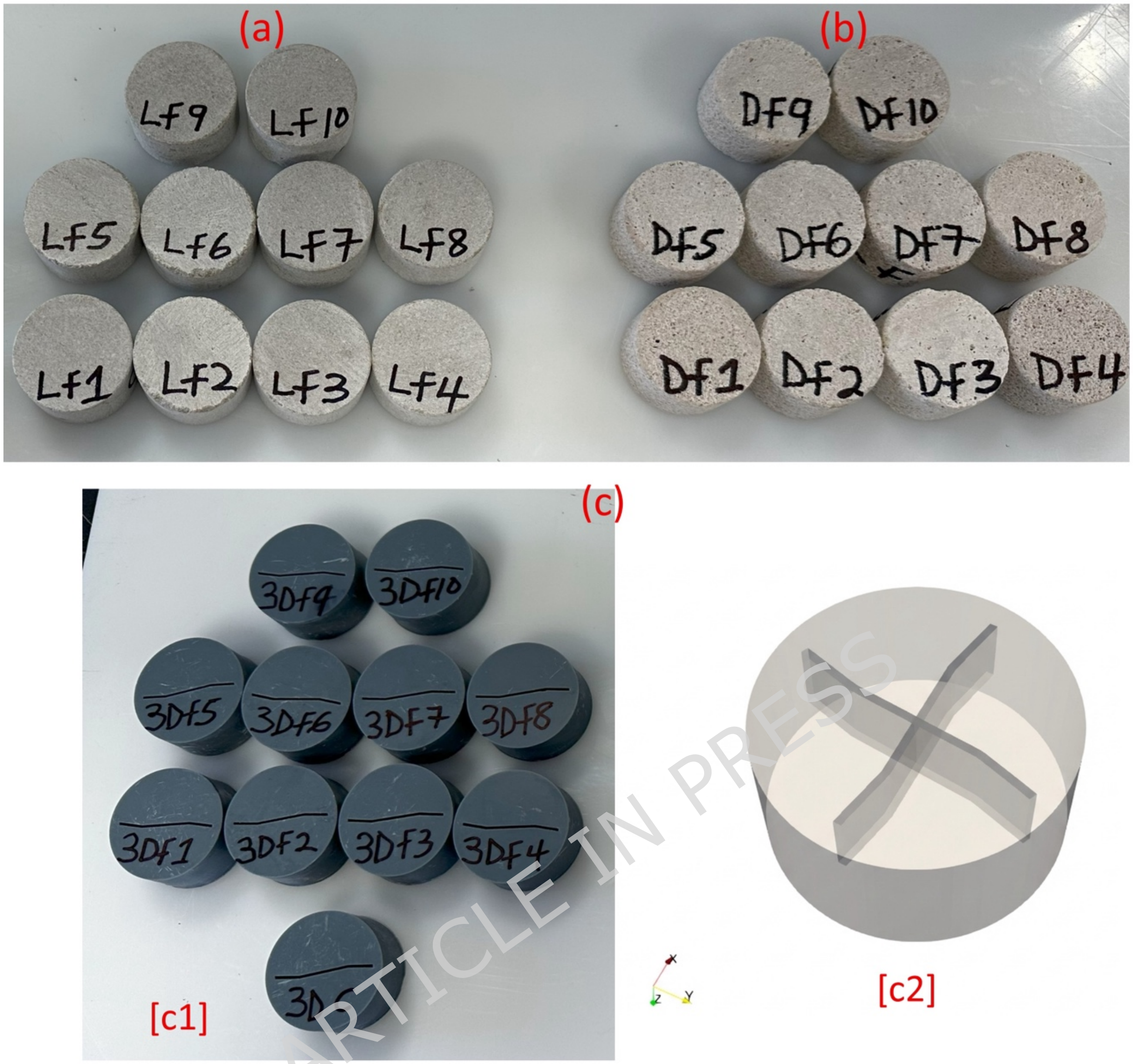

Figure 2: Rock disc samples used in this study: (a) limestone, (b) dolomite, and (c) synthetic (3D-printed) samples with [C1] actual synthetic disc samples and [C2] model of disc sample with internal fractures.

Synthetic (3D-printed) rock-like disc samples were printed using the Phrozen Sonic Mini 8K 3D Printer. The model of the rock to be printed was prepared with the same dimensions (diameter and thickness) as that of the cylindrical disc natural rock samples, but incorporating internal orthogonal fractures centrally placed to simulate fractured rock masses (Figure c), with a single fracture to serve as grout entry into the internal fractures. The rapid advancement of 3D-printing technology in rock mechanics enables the production of synthetic rock samples with independent control over size, shape, fracture orientation, aperture, and material composition (Haeri et al., 2014; Niu et al., 2023; Zhang et al., 2023a, 2023b; Yu & Tian, 2024). The synthetic disc samples incorporate more complex fracture geometries (orthogonal orientation, smaller aperture) found in fractured rock masses.

The natural rock disc samples were dried in a laboratory oven at a temperature of 60° C until there was no constant change in mass (Figure a-b), removing moisture from pore spaces, since water content can affect BDT results. All disc samples were stored in enclosed, air-tight vessels prior to grouting treatment. All the disc samples were kept in an enclosed, air-tight vessel before the grout treatments of the fractured samples.

Table 1: Rock disc sample grouping for grouting and mechanical characterization.

Sample ID	**Curing Period (hr)**	**Rock Type**	**No of Samples**	**Test Method**
LF1 – LF10	24	Limestone	10	Brazilian Test
DF1 – DF 10	24	Dolomite	10	Brazilian Test
3DC	N/A	Synthetic (3D-printed)	1	Brazilian Test (control, ungrouted)
3DF1 - 3DF10	24	Synthetic (3D-printed)	10	Brazilian Test

As required by the rock mechanics testing standard (ASTM, 2023) for accurate and reproducible BDT results, a minimum of ten disc samples per rock type was used. One synthetic disc (3DC) was designated as a control and not grouted, to provide a baseline condition for the synthetic material. For clarity in analyses in this study, synthetic rock samples (containing modeled internal fractures) and natural rock samples (with tensile fractures induced by BDT) without grouting are hereinafter referred to as *'ungrouted samples'*; whereas the natural and synthetic samples after fracture grouting are referred to as '*fracture-grouted samples*'.

2.1.2 Fracture Grouting Treatment

The grout used for fracture filling is a nanomagnetic material (herein referred to as nanomagnetic slurry), developed with nanomagnetic powder (Fe_3O4), fly ash, and epoxy resin emulsion (Fig. 3), following the procedure established by Oppong and Kolawole (2025) with a recommended mixture design of 15%

nanomagnetic material. Prior to fracture grouting, Parafilm 'M' was used to firmly wrap fractured disc samples to prevent slurry from flowing out during injection.

Figure 3: Grout materials and preparation.

During the grout treatment of the fractured samples, a laboratory syringe with a small annulus diameter (2 mm) was filled with the grout slurries to ensure easy penetration into the targeted fractures. Constant manual pressure on the syringe facilitated uniform grout flow into the fractures. Grouted disc samples were then cured in a laboratory oven at 25 ˚C for 24 hr. The parafilm was thereafter removed, and end faces were re-polished and smoothened to ensure even stress distribution and eliminate surface irregularities and errors before further testing.

2.2 Characterizing the Grouting Reinforcement Mechanism for Fractured Surrounding Rock Mass via Brazilian Disc Test

Grouting is an effective technique for filling fractures within surrounding rock masses and enhancing their mechanical integrity. To evaluate how grouting alters the tensile strength of rock mass surrounding underground excavations, the BDT was used, expressed in Eq. (1). BDT is the standardized approach for determining the tensile strength (*TS*) of rocks under a diametral or axial tensile load (Li & Wong, 2013;

Perez-Rey et al., 2023; Abdi, 2024), also referred to as the splitting tensile strength or indirect tensile strength test. The BDT procedure follows globally established standards (ISRM, 1978; ASTM, 2023). According to these standards, the stress at tensile failure (σ_t) is a function of the maximum load at failure (P), the diameter (D), and the disc thickness (t). As shown in Fig. 4, stress is applied to generate a uniform tensile stress across the loaded diameter following vertical compressive stress. When the cylindrical disc sample is diametrically subjected to P, σ_t is estimated using Eq. (1):

$$\sigma_t = \frac{2P}{\pi Dt} = 0.636\frac{P}{Dt} \quad (1)$$

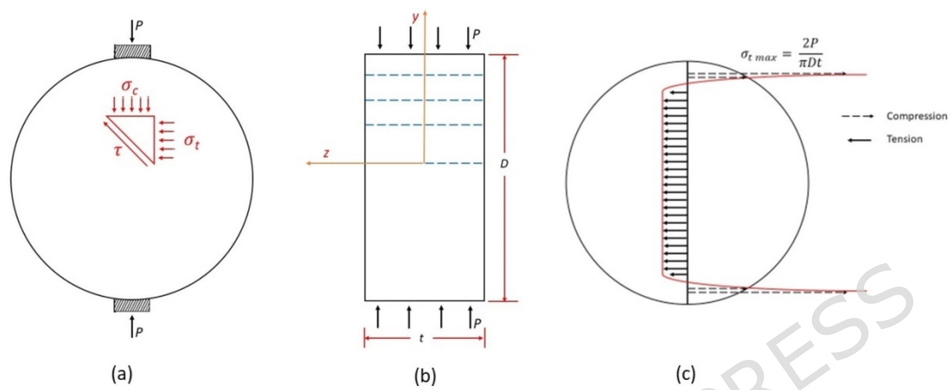

Figure 4: Illustration of tensile stress distribution generated in the rock disc samples during Brazilian disc tests (BDT).

A Triaxial rock testing system (Fig. 5) in the Geomechanics for Geo-Engineering and Sustainability (GGES) Lab at New Jersey Institute of Technology, equipped with a BDT apparatus, was used for this study. A total of 61 BDT tests were conducted, and this is comprised of: 10 limestone disc samples × 2 tests (ungrouted and fracture-grouted states) = 20 tests; 10 dolomite disc samples × 2 tests (ungrouted and fracture-grouted states) = 20 tests; 10 synthetic (3D-printed) disc samples with modeled internal fractures × 2 tests (ungrouted and fracture-grouted states) = 20 tests; 1 synthetic control disc × 1 test (ungrouted baseline) = 1 test; total = 61 BDT tests from 31 samples. A loading rate of 0.3 MPa/s was applied, within the recommended range of 0.05 to 0.35 MPa/s for tensile failure in rocks (ASTM, 2023). Samples were carefully positioned between the two loading jaws to ensure even stress distribution along the diameter, and the contact area between sample and loading jaw at failure subtends 15°, following the setup proposed by ISRM (1978). An axial stress was applied to the samples to induce tensile fractures in the samples, and the maximum stress before failure is recorded as the tensile strength (TS) of the rock.

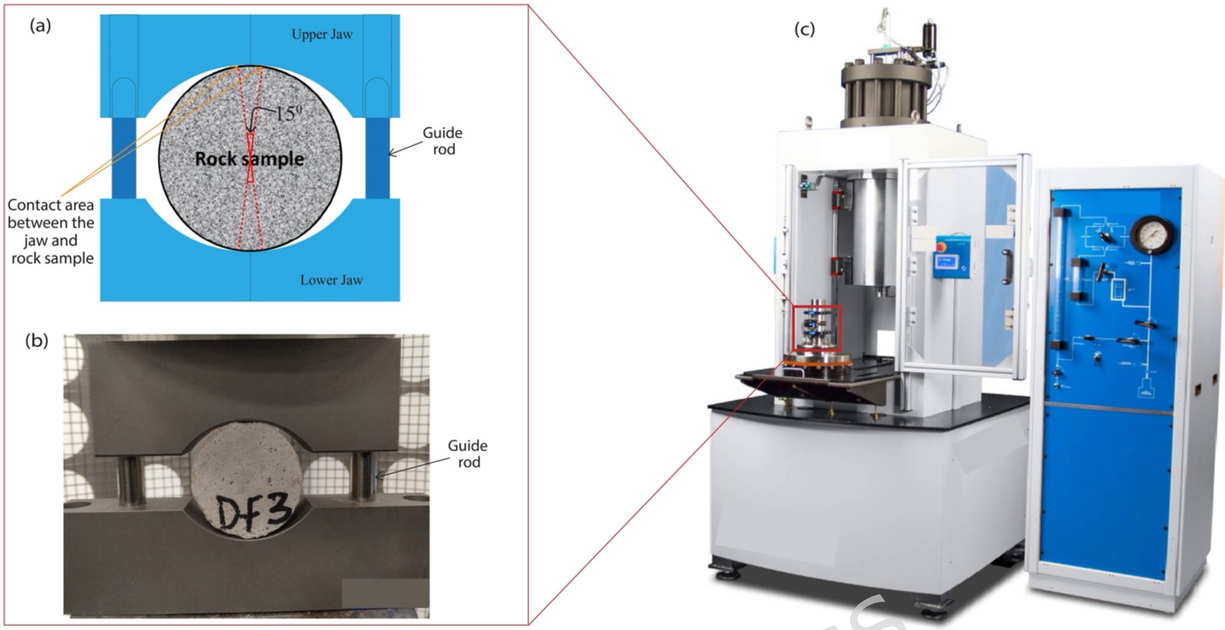

Figure 5: Brazilian disc test (BDT) configuration: (a) schematic of the test, and (b-d) actual setup.

As shown in Fig. 5, natural rock samples (limestone and dolomite) were first placed in the loading jaws and subjected to controlled loading to induce tensile fractures, simulating the first group (natural rocks) of ungrouted rock mass samples. The first BDT was terminated immediately upon the initial significant drop in applied axial load, corresponding to primary tensile fracture initiation (failure onset). This criterion was consistently applied across all 20 natural rock specimens. The synthetic rock samples (3DF1-3DF10) with internally modeled orthogonal fractures were tested in their ungrouted state as the second group of ungrouted rock mass samples, then prepared for grouting.

TFL refers to the cumulative length of all visible fractures within a tested sample, measured individually and summed after failure. For repeatability, measurement of *TFL* required that the test be stopped immediately upon the initial drop in applied stress. At this stage, the fracture pattern was photographically characterized and the fracture lengths were measured. Specifically, immediately upon failure initiation, specimens were carefully removed from the loading jaws and photographed from both flat disc faces under controlled, consistent lighting. All visible tensile fracture traces were manually digitized on calibrated digital images using ImageJ (version 1.54, NIH), with scale calibrated using the known specimen diameter (38.1 mm for natural and control samples). Both primary and secondary (branch or wing) fractures that were visually distinguishable and measurable were included. Surface spalling at jaw contact zones was excluded, as these represent locally compressive zones. *TFL* was computed as the sum of all individual fracture lengths on both disc faces, then normalized per face (mm per specimen). *TFL* measurements were performed independently by two researchers, with results agreeing within 5%, demonstrating acceptable reproducibility.

For the fracture-grouted BDT (second BDT), each specimen was repositioned in the loading jaws such that the pre-existing grouted fracture plane was oriented perpendicular to the applied diametral load (that is, the fracture plane was parallel to the loading direction), ensuring that the applied tensile stress acted across the grouted fracture interface. This loading orientation is rotated 90° relative to the orientation used to induce the original tensile fracture in the first BDT, and represents the condition most relevant to assessing grouting reinforcement under tensile stress in underground environments. It is important to note that fracture-grouted specimens represent new rock-grout composite systems rather than restored versions of the original intact rock: after BDT-induced fracture, specimens undergo irreversible changes (fragment separation, fracture surface relief, microcrack extension), and the second BDT therefore tests a heterogeneous composite rock system whose mechanical response is governed by grout-rock interface properties, fracture aperture distribution, and stiffness contrasts. This rock composite-specimen nature is an inherent feature of the experimental design and is considered in interpreting results.

Subsequently, fractured natural rock disc samples were removed from the loading jaws and prepared for grouting treatment. Fractured samples (both natural and synthetic) were tightly wrapped with parafilm to maintain their disc-like structure. Fractures in the parafilm-wrapped natural rock samples were injected with grouting slurry. The modeled internal fractures of synthetic disc samples were injected with grouting slurry through the surface-exposed fracture. BDT was thereafter conducted on all fracture-grouted samples.

2.3 Numerical Simulation Framework: FEM-CZM

To mechanistically interpret and extend the experimental observations, a two-dimensional finite element model employing the cohesive zone method (FEM-CZM) was developed and implemented using ABAQUS (Park & Paulino, 2013; ABAQUS, 2021, 2026). This numerical framework explicitly simulates the initiation and propagation of micro-fractures in Brazilian disc specimens, providing direct visualization of stress concentration evolution, damage onset, and fracture-path control in ungrouted fractured and fracture-grouted disc specimens. The FEM-CZM approach was selected because it accurately describes the continuity and discontinuity of rock materials, captures the damage evolution process prior to fracture, and predicts crack initiation, propagation path, and ultimate fracture behavior with high fidelity (Han et al., 2020, 2022; Du et al., 2021; Asadizadeh et al., 2025). An advantage of the FEM-CZM approach is that the cohesive zone at the fracture interface explicitly models the traction-separation behavior, enabling simulation of both the pre-failure stiffness of the rock-grout system and the progressive damage that controls failure mode and fracture path.

2.3.1 Model Geometry and Mesh

The model geometry replicates the experimental specimen dimensions: circular disc with diameter $D = 38.1$ mm and thickness $t = 19.1$ mm, simplified to a 2D plane-stress model consistent with prior BDT simulations in the literature (Zhou et al., 2021; Du et al., 2021; Asadizadeh et al., 2025). A 2D plane-stress formulation is appropriate for disc specimens that are thin relative to their diameter ($t/D = 0.5$), and this approximation has been validated against 3D simulations and experimental results for BDT by Zhu and Tang (2006) and Saksala et al. (2013). A single central fracture of length $2a = 15$ mm (representing the natural tensile fracture induced in natural rock specimens during the first BDT) was introduced at the specimen center, oriented along the vertical loading direction (Fig. 6a). Loading was applied through rigid platens (jaw width = 6 mm, conforming to experimental conditions) via displacement control at the upper jaw, with the lower jaw fixed.

The bulk disc was discretized using four-node bilinear plane-stress elements with reduced integration and hourglass control (CPS4R). A refined mesh with element size $h_{max} = 0.5$ mm was used in the vicinity of the fracture and in the expected fracture process zone, with a coarser mesh ($h_{max} = 2$ mm) in the bulk away from the fracture (Fig. 6b). The fracture interface was modeled using zero-thickness cohesive elements (COH2D4), embedded at the fracture plane between duplicate nodes generated by splitting the mesh at the fracture surfaces (Fig. 6c). This zero-thickness formulation ensures that nodal separation displacement equals the nominal cohesive strain, and the constitutive thickness of cohesive elements was set to 1.0 with geometric thickness = 0, following established practice (Han et al., 2020a, 2020b). Contact between loading platens and the disc surface was defined as surface-to-surface with hard normal contact and frictionless tangential behavior. Displacement increments of $\delta_u = 0.001$ mm per step were applied monotonically until complete specimen failure.

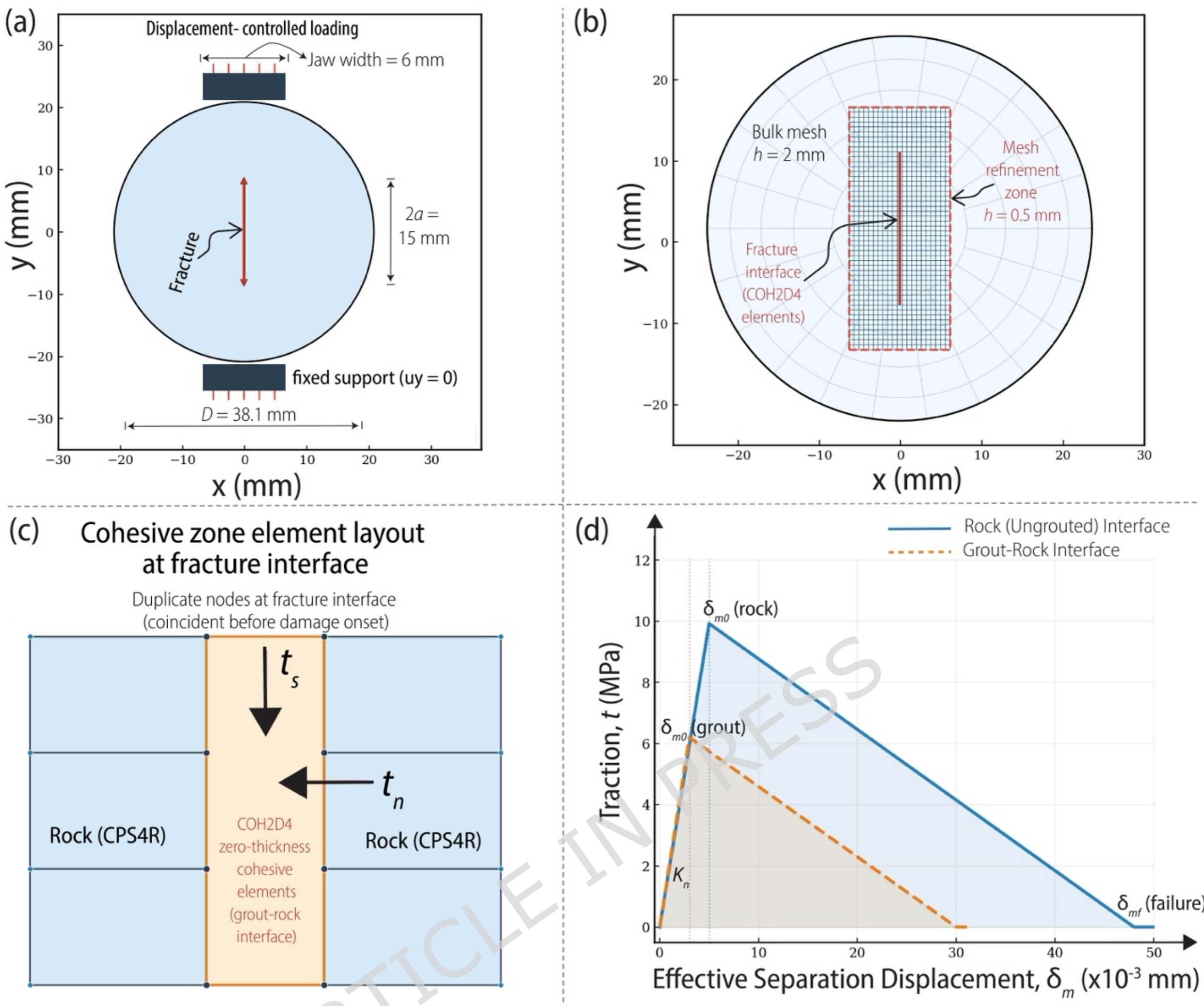

Figure 6: Numerical simulation model development: (a) geometry and boundary conditions of the BDT disc specimen with central fracture, (b) mesh refinement around the fracture interface, (c) cohesive element layout at the fracture interface, and (d) schematic of the bilinear traction-separation law used for the cohesive zone.

2.3.2 Constitutive Model and Material Parameters

The bulk disc material (limestone and dolomite) was modeled as a linear elastic isotropic continuum, appropriate for brittle rocks under quasi-static BDT loading, where the bulk material outside the fracture process zone remains largely elastic. Rock failure in the bulk (outside the predefined cohesive zone) was not explicitly modeled, as the experimental and simulation focus is on the fracture behavior along the pre-existing fracture interface and the grout-rock interface. The cohesive zone at the fracture interface follows the bilinear traction-separation law (Fig. 6d) implemented in ABAQUS, which exhibits linear elastic hardening prior to damage onset and linear softening after damage initiation (Du et al., 2021; Han et al., 2020b). The traction-separation law governing the cohesive element response is expressed as:

$$t = \begin{Bmatrix} t_n \\ t_s \\ t_t \end{Bmatrix} = \frac{I}{L}\begin{vmatrix} E_{nn} & E_{ns} & E_{nt} \\ E_{ns} & E_{ss} & E_{st} \\ E_{nt} & E_{st} & E_{tt} \end{vmatrix}\begin{Bmatrix} \delta_n \\ \delta_s \\ \delta_t \end{Bmatrix} = \begin{vmatrix} K_{nn} & K_{ns} & K_{nt} \\ K_{ns} & K_{ss} & K_{st} \\ K_{nt} & K_{st} & K_{tt} \end{vmatrix}\begin{Bmatrix} \delta_n \\ \delta_s \\ \delta_t \end{Bmatrix} \quad (2)$$

where t_n, t_s, and t_t are the normal and two shear traction components (MPa); δ_n, δ_s, and δ_t are the corresponding separation displacements (mm); K is the stiffness matrix (MPa/mm); and L is the constitutive thickness (which is 1.0 mm); and I is the identity scalar.

The Macaulay bracket formulation (damage softening phase) ensures rock damage occurs only under tensile loading. The normal traction (t_n) and the shear traction (t_s or t_t) components during damage evolution are expressed as:

$$t_n = \begin{cases} (1 - D)\, t_{n0}\,, & t_{n0} \geq 0 \text{ (tension)} \\ t_{n0}\,, & t_{n0} < 0 \text{ (compression, no damage)} \end{cases} \quad (3)$$

$$t_s = (1 - D)t_{s0}\,; \quad t_t = (1 - D)t_{t0} \quad (4)$$

where D is the scalar damage variable evolving from 0 (D = 0 = undamaged) to 1 (D = 1 = fully failed, element deleted), governed by the BK (Benzeggagh-Kenane) mixed-mode fracture energy criterion [G_c]; t_{s0} and t_{t0} are the undamaged shear tractions at the current separation; both degrade identically with the same scalar damage variable D. The damage variable D modifies the element stiffness, and elements with $D = 1$ are deleted (element removal) to represent a complete fracture. Damage initiates when the maximum nominal stress damage initiation criterion is satisfied (i.e., when maximum traction ratio reaches unity in any mode):

$$\max\left\{\frac{\langle t_n \rangle}{t_n^0}, \frac{t_s}{t_s^0}, \frac{t_t}{t_t^0}\right\} = 1 \quad (5)$$

where t_n^0 is the peak normal traction strength (MPa); t_s^0, t_t^0 are the peak in-plane and out-of-plane shear traction strengths (MPa). < > denotes the Macaulay bracket, and it ensures that damage evolution will occur only under the tensile effect. Damage evolution follows as:

$$D = \frac{\delta_{mf}(\delta_{mm} - \delta_{m0})}{\delta_{mm}(\delta_{mf} - \delta_{m0})} \quad (6)$$

where δ_{mm} is the maximum effective displacement reached during loading history (mm); δ_{m0} is the effective displacement at damage onset (mm); and δ_{mf} is the effective displacement at complete failure (mm), related to the mixed-mode fracture energy G_c via the BK criterion (mm); and δ_m is the effective mixed-mode displacement, which is mathematically expressed as:

$$\delta_m = \sqrt{\langle \delta_n \rangle^2 + \delta_s^2 + \delta_t^2} \quad (7)$$

Similarly, the BK mixed-mode critical fracture energy at failure (which governs δ_{mf} in Eq. 6) is mathematically defined as:

$$G_C = G_{nC} + (G_{sC} - G_{nC})\left[\frac{G_S + G_T}{G_N + G_S + G_T}\right]^{\eta} \quad (8)$$

where G_C is the total mixed-mode critical fracture energy at failure (N/mm = kJ/m²); G_{nC} is the Mode-I (opening) critical fracture energy, i.e., fracture energy under pure normal separation (N/mm); G_{sC} is the Mode-II (in-plane shear) critical fracture energy, i.e., fracture energy under pure in-plane shear separation (N/mm); G_N is the Mode-I fracture energy dissipated at the current loading state, i.e., work done by normal traction t_n over normal separation δ_n (N/mm); G_S is the Mode-II fracture energy dissipated at the current loading state, i.e., work done by in-plane shear traction t_s over shear separation δ_s (N/mm); G_T is the Mode-III fracture energy dissipated at the current loading state, i.e., work done by out-of-plane shear traction t_t over shear separation δ_t (N/mm); ≈ 0 in 2D plane-stress models; η is the BK material exponent which controls the shape of the mixed-mode failure locus (dimensionless), η = 1.45 for all interfaces (Table 2).

Material properties for the numerical models were calibrated against the mean experimental *TS* values, and reference was made to established values in the literature for these rock types (Table 2). The elastic moduli and Poisson ratios for limestone and dolomite were taken from published values (Gueguen & Palciauskas, 1994; Salimian et al., 2017; Hu et al., 2024). Cohesive zone parameters (peak traction strengths and fracture energy) were calibrated by iterative simulation until the simulated load-displacement curves and peak loads matched the experimental means within 5%. For the ungrouted fractured model, the cohesive elements represent the open tensile fracture surfaces with minimal residual cohesion. For the fracture-grouted model, the cohesive elements represent the grout-rock interface, with material properties characteristic of the nanomagnetic slurry grout (epoxy resin emulsion base with fly ash and Fe_3O_4 filler), calibrated against the experimental fracture-grouted *TS* results. Table 2 summarizes all material input parameters used in the numerical models.

Table 2: Input parameters used in FEM-CZM numerical simulations.

Parameter	**Limestone**	**Dolomite**	**Nanoparticles-based Grout**	**Reference**
Elastic Modulus, *E* (GPa)	46	40	4.5	Gueguen & Palciauskas, 1994; Oppong & Kolawole, 2025; Sonibare et al., 2026
Poisson's Ratio, ν (-)	0.25	0.28	0.30	Gueguen & Palciauskas, 1994

Normal Peak Traction, t_{n0} (MPa)	9.92	7.50	6.20	Calibrated (this study)
Shear Peak Traction, t_{s0} (MPa)	19.84	15.00	12.40	Calibrated (this study)
Normal Fracture Energy, G_{nC} (kJ/m^2 or N/mm)	0.055	0.042	0.028	Calibrated; Han et al., 2020b
Shear Fracture Energy, G_{sC} (kJ/m^2 or N/mm)	0.110	0.084	0.056	Calibrated; Han et al., 2020b
Initial Cohesive Stiffness, K_n (GPa/m)	1000	800	500	Han et al., 2020a, 2020b
Density, ρ (kg/m^3)	2600	2850	1750	Gueguen & Palciauskas, 1994
BK Mixed-Mode Exponent, η (-)	1.45	1.45	1.45	Han et al., 2020b

2.3.3 Simulation Cases

Four (4) simulation cases were executed in this study to directly parallel and extend the experimental conditions: Case 1 = ungrouted limestone disc with central fracture under BDT; Case 2 = fracture-grouted limestone disc (grout properties at fracture interface) under BDT; Case 3 = ungrouted dolomite disc with central fracture under BDT; and Case 4 = fracture-grouted dolomite disc under BDT. For each case, the outputs that were extracted include load-displacement response (for comparison with experimental BDT load-displacement curves and *TS* values); damage variable distribution (*D*) and stress contour (maximum principal stress, σ_{max}) at key loading stages (25%, 50%, 75%, and 100% of peak load); fracture path length and propagation trajectory; and Mode-I vs. Mode-II fracture energy dissipation ratio. Simulation results were compared with experimental *TS*, *TFL*, and failure mode data to validate the model and interpret the physical mechanisms.

3 Results

3.1 Tensile Strength of Ungrouted Rock Samples

The *TS* of the ungrouted rock samples is presented in Table 3. The mean *TS* across each rock type indicates that limestone discs yielded the highest mean *TS* of 9.92 MPa, dolomite discs produced a relatively lower mean *TS* of 7.50 MPa, and the lowest mean *TS* was recorded in the synthetic rock disc (7.23 MPa, from control specimen 3DC). The tensile fractures generated in natural rock samples appeared to be of larger aperture than the internally modeled fractures in synthetic fractured rock samples, illustrating the value of synthetic samples for characterizing fracture-grouted rocks with smaller fracture aperture.

Table 3: Tensile strength results of ungrouted rock samples.

Sample No	**Tensile strength, *TS* (MPa)**		
	Limestone rock samples	***Dolomite rock samples***	***Synthetic rock samples***
1	10.36	8.06	7.23
2	10.12	7.79	7.23
3	9.69	8.12	7.23 7.23
4	9.03	6.68	7.23
5	10.47	8.44	7.23
6	8.87	7.13	7.23 7.23
7	9.88	6.88	7.23
8	10.86	8.44	7.23
9	9.60	6.27	7.23
10	10.35	7.18	7.23
Mean	**9.92**	**7.50**	**7.23**

Note: Synthetic rock sample value (Sample 1) represents the single control specimen (3DC). All 10 synthetic specimens with modeled internal fractures were tested in BDT before grouting as the second group of ungrouted samples; control specimen 3DC serves as a representative baseline.

3.2 Fracture-Grouting of Rock Mass Samples

As shown in Fig. 7, the slurry-filled fractures in all grouted samples. The tensile-induced fractures in natural rock samples (Fig. 7a-b) and the internally-modeled intersecting fractures in synthetic fractured rock samples (Fig. 7c) were grouted with nanomagnetic slurry, confirming successful infilling of rock fractures. After grouting and curing, the fracture-grouted samples were subjected to tensile stress via BDT to obtain post-grouting TS and characterize fracture behavior.

Figure 7: Fracture-grouted rock samples after successful grouting: (a) dolomite rock samples, (b) limestone rock samples, and (c) synthetic rock samples.

3.3 Tensile Strength of Fracture-Grouted Rock Samples

After treatment, fracture-grouted samples were subjected to tensile stress via BDT with the grouted fracture plane oriented perpendicular to the applied axial load. The estimated *TS* of the fracture-grouted samples is presented in Table 4. Limestone samples attained the highest mean *TS* of 9.16 MPa after fracture grouting, dolomite samples exhibited the lowest mean *TS* of 6.00 MPa, and synthetic discs (with smaller fracture aperture and intersecting fractures) yielded a mean TS of 7.97 MPa after grouting, higher than the dolomite post-grouting mean but lower than the limestone post-grouting mean. It should be noted that Sample LF3 (limestone, fracture-grouted) yielded a *TS* of 28.19 MPa, which is substantially higher than all other fracture-grouted limestone values and considerably exceeds the original ungrouted *TS* of 9.69 MPa for the same specimen. Thorough review of the raw load-displacement record confirms this measurement was technically valid (identical loading conditions, well-defined symmetric loading curve, no apparatus anomalies). This anomalously high value likely reflects a particularly effective localized grout-reinforcement arrangement unique to this specimen, where fracture orientation and grout distribution produced highly efficient load bridging across the fracture interface. Such variability is documented in BDT studies on grouted or heterogeneous specimens (Salimian et al., 2017; Hu et al., 2024) and is consistent with the inherent variability of fracture-grout composite systems. This data point is retained as a legitimate measurement; excluding it reduces mean grouted limestone TS from 9.16 to approximately 7.05 MPa, consistent with an overall pattern of partial tensile strength recovery.

Table 4: Tensile strength results of fracture-grouted rock samples

Sample No	**Tensile strength, *TS* (MPa)**		
	Limestone samples	***Dolomite samples***	***Synthetic samples***
1	11.33	7.02	8.07
2	7.83	6.23	8.35
3	28.19	4.73	8.68
4	6.93	5.82	7.91
5	4.73	5.79	8.32
6	5.79	7.40	7.54
7	6.29	5.81	7.70
8	7.28	6.40	7.91
9	5.27	3.59	7.32
10	8.01	7.18	7.90
Mean	**9.16**	**6.00**	**7.97**

LF3 (limestone, fracture-grouted) is a statistically anomalous value (28.19 MPa) attributed to particularly efficient grout bridging. Excluding this value, the mean grouted limestone TS = 7.05 MPa.

3.4 Total Fracture Length (TFL) of Fracture-Grouted Rock Samples

Total Fracture Length (*TFL*) refers refers to the cumulative length of all visible tensile fractures within a given rock disc sample, measured individually and summed. This parameter was adopted to quantitatively evaluate the extent of tensile fracture development in rock masses under tensile stress, as previously described. This parameter does not apply to synthetic rock samples in this study, as no visible fractures were observed after tensile failure of those samples. The *TFL* for five (5) samples per condition of the ungrouted and fracture-grouted natural rock samples with measurable fractures was evaluated alongside corresponding *TS* values, as presented in Table 5. *TFL* for ungrouted limestone discs ranged from 43 mm to 78 mm, and for fracture-grouted limestone discs from 38 mm to 71 mm. *TFL* of ungrouted dolomite discs ranged from 16 mm to 79 mm, and fracture-grouted dolomite discs from 33 mm to 68 mm.

Table 5: The tensile strength (*TS*) and total fracture length (*TFL*) for ungrouted and fracture-grouted natural rock samples.

Rock Type	**Grouting condition**	***TS* (MPa)**	***TFL* (mm)**
Limestone	Ungrouted	10.36	73
		10.12	52
		9.69	43
		9.03	59
		10.47	78
	Fracture-grouted	11.33	71
		7.83	67
		28.19	38
		6.93	70
		4.73	48
Dolomite	Ungrouted	8.06	48
		7.79	52
		8.12	16
		6.68	42
		8.44	79
	Fracture-grouted	7.02	35
		6.23	68
		4.73	46
		5.82	33
		5.79	44

3.5 Numerical Simulation: Tensile Strength Evolution and Micro-Fracture Initiation and Propagation

The FEM-CZM simulations produced distinct mechanical responses and fracture evolution behavior for the four model cases (ungrouted and fracture-grouted limestone and dolomite disc specimens) in this study. The simulations provide direct mechanistic insight into the experimental values and observations, enabling interrogation of processes that are inaccessible from experimental observation alone. The key results are presented and discussed, with direct comparison to the experimental data.

3.5.1 Validation: Simulated vs. Experimental Load-Displacement Responses and Tensile Strength

Fig. 8 presents a comparison of the simulated load-displacement curves with the experimental BDT results for ungrouted and fracture-grouted limestone (Cases 1 and 2) and dolomite (Cases 3 and 4) specimens. The simulated load-displacement responses exhibit the characteristic three-stage behavior: (i) an initial non-linear hardening phase attributed to contact compaction and micro-crack closure; (ii) a linear elastic phase;

and (iii) a sharp post-peak softening phase corresponding to rapid fracture propagation and specimen failure. This three-stage response pattern is consistent with the experimental observations.

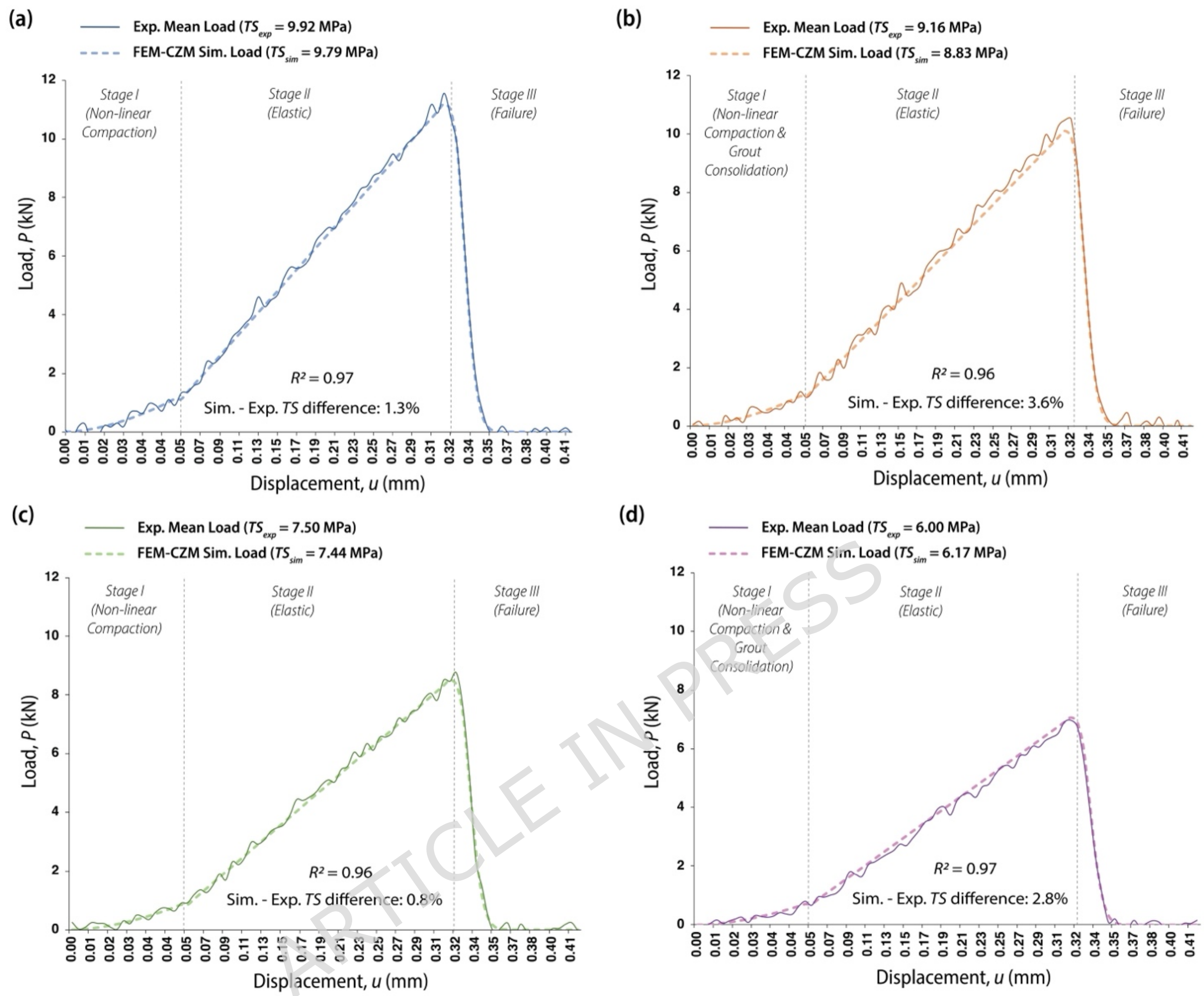

Figure 8: Validation of simulated and experimental load-displacement responses for BDT of (a) ungrouted limestone [Case 1], (b) fracture-grouted limestone [Case 2], (c) ungrouted dolomite [Case 3], and (d) fracture-grouted dolomite [Case 4] specimens.

For ungrouted limestone (Case 1), the simulated peak load yielded a *TS* of 9.79 MPa, compared to the experimental mean of 9.92 MPa (difference: 1.3%). For ungrouted dolomite (Case 3), the simulated *TS* was 7.44 MPa against the experimental mean of 7.50 MPa (difference: 0.8%). For fracture-grouted limestone (Case 2), the simulated *TS* was 8.83 MPa compared to the experimental mean of 9.16 MPa (difference: 3.6%). For fracture-grouted dolomite (Case 4), the simulated *TS* was 6.17 MPa against the experimental mean of 6.00 MPa (difference: 2.8%). All simulated *TS* values agree with the experimental means within 4%, demonstrating satisfactory model calibration. The simulated post-peak load decay and failure displacement also closely match the experimental observations, as summarized in Table 6.

Table 6: Tensile strength (*TS*) validation.

Specimen Condition	Experimental Mean *TS* (MPa)	Simulated Mean *TS* (MPa)	Simulation-Experimental *TS* Difference (%)	R^2
Ungrouted Limestone	9.92	9.79	1.3	0.97
Fracture-grouted Limestone	9.16*	8.83	3.6	0.96
Ungrouted Dolomite	7.50	7.44	0.8	0.96
Fracture-grouted Dolomite	6.00	6.17	2.8	0.97

**Value includes all fracture-grouted limestone specimens, including the anomalous LF3 specimen. R^2 indicates the coefficient of determination for the fit between simulated and experimental load-displacement curves.*

3.5.2 Stress Concentration and Damage Simulation

Fig. 9 presents the maximum principal stress (σ_{11}) and damage variable (D) contour plots at three loading stages (50%, 75%, and 100% of peak load) for representative ungrouted and fracture-grouted disc specimens, with the key FEM-CZM simulation results summarized in Table 7. These results provide direct visualization of the evolution of stress concentration and progressive damage that cannot be obtained directly from the experimental measurements.

For the ungrouted limestone disc (Case 1), high tensile stress concentrations develop at the fracture tips immediately upon load application. By 50% of peak load, principal stresses at the fracture tips approach the cohesive zone peak traction (approximately 9.8 MPa), and localized damage ($D > 0.1$) initiates at both crack tips [Fig. 9(a- i)]. At 75% peak load, the damage zone expands radially from the crack tips along the loading axis, and at peak load, complete damage ($D = 1$) defines a through-crack that connects the original fracture tips to the specimen boundaries [Fig. 9(a-ii, iii)]. This fracture path corresponds to the single- or multiple-axial splitting failure modes observed experimentally in ungrouted specimens. The total simulated fracture path length at failure was 29.7 mm, consistent with the experimental *TFL* range of 43-78 mm (the difference reflecting that the simulation tracks only the primary through-crack, while experimental *TFL* includes all visible secondary branches). For the fracture-grouted limestone disc (Case 2), the stress distribution at early loading stages is markedly different from the ungrouted case (Fig. 9b). The grout-filled fracture acts as a mechanical bridge, redistributing tensile stresses more uniformly across the disc cross-section and reducing peak stress concentrations at the fracture tips by approximately 38% at 50% peak load compared to the ungrouted condition (6.1 MPa vs. 9.8 MPa at the crack tip, respectively). Damage initiation is delayed ($D > 0.1$ first appears at 71% of peak load, compared to 50% in the ungrouted case), and the subsequent damage propagation is more tortuous, deviating from the vertical loading axis in response to the grout-rock interfacial constraint. The simulated fracture path at failure shows crack deflection and bifurcation near the grout-rock boundary, consistent with experimentally observed mixed failure-mode transitions in grouted specimens [Fig. 9(b-iii)]. The simulated *TFL*-equivalent fracture path length at failure was 22.4 mm, representing a reduction of approximately 25% compared to the ungrouted case, consistent with the experimentally observed reduction in *TFL* after grouting.

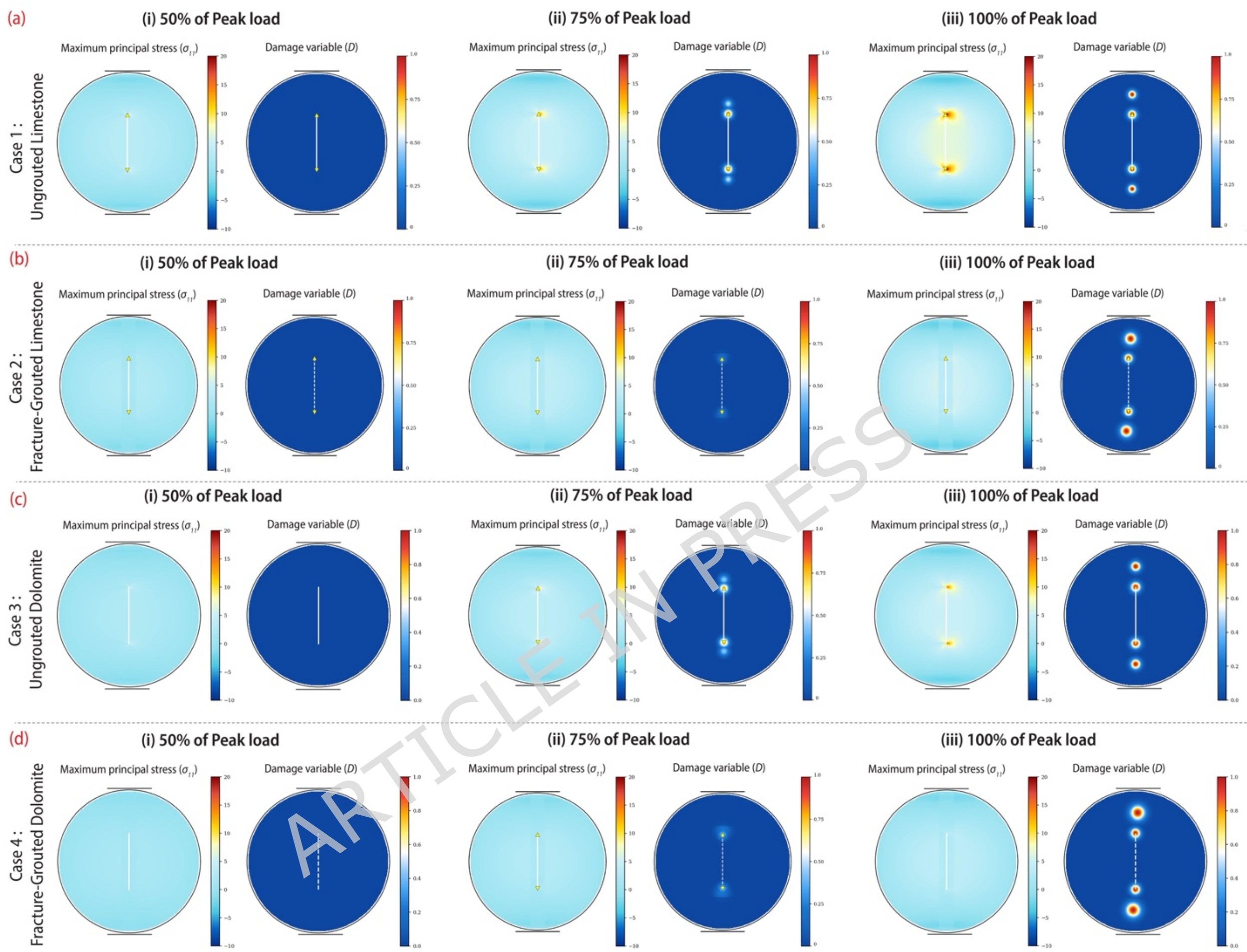

Figure 9: Contour plots of maximum principal stress and damage variable (D) at three loading stages (50%, 75%, and 100% of peak load) for: (a) ungrouted limestone (Case 1), and (b) fracture-grouted limestone (Case 2). [Red colors indicate high tensile stress or high damage; Scale bar = 5 mm].

Table 7: Key numerical simulation results compared with experimental results and observations.

Parameter	Ungrouted Limestone (Simulated)	Fracture-Grouted Limestone (Simulated)	Ungrouted Dolomite (Simulated)	Fracture-Grouted Dolomite (Simulated	Experimental (Exp.) Range / Observation
A. Fracture Path Length					
Simulated primary fracture path (mm)	29.7	22.4	27.1	19.8	*Exp. TFL: 43–78 (Ungrouted); 38–71 (Fracture-gtouted) [includes all visible branches]*
Fracture path reduction after grouting (%)	—	24.6	—	26.9	*Exp. mean TFL reduction: ~18–23% (Limestone); ~22–30% (Dolomite)*
B. Damage Initiation					
Damage initiation load (% of peak)	50	71	55	68	*Not directly measurable experimentally; consistent with Fig. 9*
Delay in damage onset due to grouting (% pts)	—	+21	—	+13	*Smaller delay for dolomite: weaker grout–dolomite bond vs. limestone*
C. Mode-I / Mode-II Fracture Energy Dissipation					
Mode-I energy fraction (%)	84	74	82	71	*Consistent with observed failure in ungrouted vs. grouted samples*
Mode-II energy fraction (%)	16	26	18	29	*Highest Mode-II for Case 4; reflects increased mixed-mode*
Mode-II increase due to grouting (% pts)	—	+10	—	+11	*Slightly larger increase for fracture-grouted dolomite than limestone*
D. Fracture-tip Stress Concentration					
Fracture-tip stress reduction due to grouting (%)	—	38	—	31	*Not directly measured; consistent with reduced TFL and constrained failure behavior; lower reduction for dolomite reflects smaller grout–rock stiffness contrast*
E-factor (E_{rock} / E_{ref})	1.000	1.000	0.870	0.870	*E_{factor} drives K_I difference, process zone width, and stress-reduction magnitude*

Analogous but quantitatively distinct behavior was observed for dolomite specimens (Cases 3 and 4), as shown in Fig. 9c-d. The adoption of a shared σ_{11} colorbar scale (σ_{max} = 20 MPa) across all four cases simulated, enabling direct visual comparison of absolute stress magnitudes between lithologies, and the results confirm that dolomite rock sustains systematically lower stress field intensities, consistent with its lower elastic modulus (E = 40 GPa vs. 46 GPa) and lower peak traction strength (7.44 MPa vs. 9.79 MPa). For ungrouted dolomite specimens (Case 3), fracture-tip stress concentrations at 50% of peak load are approximately 14% lower than the corresponding limestone values, attributable to the elastic modulus ratio ($E_{dolomite}/E_{limestone}$ = 0.870) reducing K_{I}, and the stress concentration zone is visibly broader and more diffuse, reflecting a longer fracture process zone [Fig. 9 (c-i)]. Damage initiates at 55% of peak load, representing a 5 percentage-point delay relative to ungrouted limestone, and propagates as a vertical through-crack at failure, consistent with the experimentally observed tensile failure modes. The simulated primary fracture path length at failure was 27.1 mm, consistent with the experimental *TFL* range for ungrouted dolomite (Table 4). For fracture-grouted dolomite (Case 4), the grout-rock interface reduces fracture-tip stress concentrations by approximately 31% relative to ungrouted dolomite [Fig. 9(d-i) vs. Fig. 9(c-i)], a smaller reduction than the 38% observed in grouted limestone, attributable to the lower stiffness contrast between the nanomagnetic grout and dolomite specimens. Damage initiation is delayed to 68% of peak load, a 13 percentage-point delay compared to ungrouted dolomite, which is less pronounced than the 21 percentage-point delay in limestone, consistent with the weaker grout-dolomite interfacial bonding evidenced by the larger experimental *TS* reduction in dolomite after grouting (approximately 20.2% vs. approximately 7.6% for limestone). The simulated fracture path at failure (19.8 mm) represents a 27% reduction relative to ungrouted dolomite, consistent with the experimentally observed *TFL* reduction (Table 4), and shows the crack deflection at the grout-rock boundary characteristic of the tensile failure modes observed experimentally.

4 Discussion

4.1 Tensile Strength and Rock-Specific Responses of Fracture-Grouted Rocks

Across lithologies, the *TS* obtained from fracture-grouted specimens remained below the intact baselines (ungrouted condition) of the same rock disc samples, indicating non-restoration of the inherent tensile strength of the rocks. It is important to note that this comparison is made between original intact rock (first BDT) and the same specimen after fracture and grouting (second BDT); the fracture-grouted specimen represents a new heterogeneous composite rock system comprising original rock fragments, grout infill, and newly formed grout-rock interfaces. This composite nature inherently introduces mechanical heterogeneity and localized stiffness contrasts that govern tensile response differently from intact rock. Despite this, grouting of tensile fractures demonstrates improved reinforcement in mechanical integrity by impeding fracture initiation and propagation, evidenced by a shift in tensile-induced failure modes toward patterns consistent with fracture arrest or deflection at rock-grout interfaces. These outcomes align with the role of grout in fracture sealing and bridging, and redistributing stresses in discontinuous porous media, even when the absolute *TS* of intact rock is not recovered.

The variation in *TS* results for all rock samples subjected to tensile stress in both ungrouted and fracture-grouted conditions is illustrated in the streamgraph (Fig. 10), which provides an overview of the distribution and variation of *TS* determined from BDT. It is important to note that in Fig. 10, the vertical dimension of each band represents the relative distribution and variation of *TS* across samples and conditions; absolute *TS* values for each condition are reported in Tables 3 and 4. The plot demonstrates that

TS values obtained from BDT are generally consistent within each condition and rock type, with the exception of an outlier observed in the fracture-grouted limestone samples (Sample LF3). This consistency suggests that BDT results for fracture-grouted underground rocks are typically reliable within the same lithology and give reproducible surrounding reinforcement performance. The FEM-CZM simulations further support these trends: the simulated *TS* reductions after grouting (9.79 to 8.83 MPa for limestone, 7.44 to 6.17 MPa for dolomite, Table 6) are in good agreement with the experimentally observed reductions, confirming that the mechanical contrast between the intact rock and the grout-rock interface governs the degree of tensile strength recovery

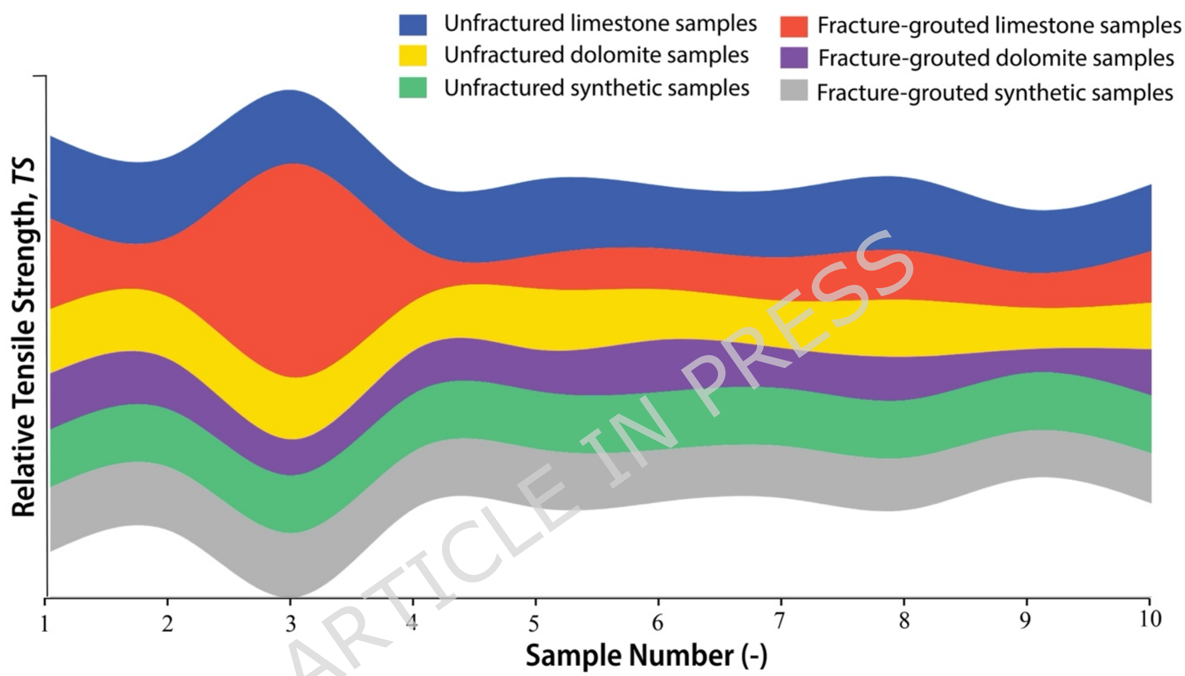

Figure 10: Streamgraph showing the distribution and variation of tensile strength (*TS*) results across all rock types and grouting conditions. [The vertical dimension of each band represents relative *TS* distribution; absolute values are in Tables 3 and 4].

Following the validation of *TS* consistency via streamgraph analysis, the influence of grout treatment on the tensile-driven mechanical response of the tested rock types was evaluated. Specifically, mean *TS* values for limestone, dolomite, and synthetic discs were compared before and after grout treatment (Fig. 11). Among the three rock types, limestone disc samples consistently exhibited the highest mean *TS* in both fracture-grouted and ungrouted conditions, while dolomite disc samples showed the lowest mean *TS* post-grouting. In contrast, the synthetic disc samples yielded the lowest mean *TS* in the ungrouted state, but demonstrated a notable tensile strength increase after grouting. These trends emphasize the rock-typedependent performance of fracture grouting and the importance of intrinsic rock fabric in governing tensile response.

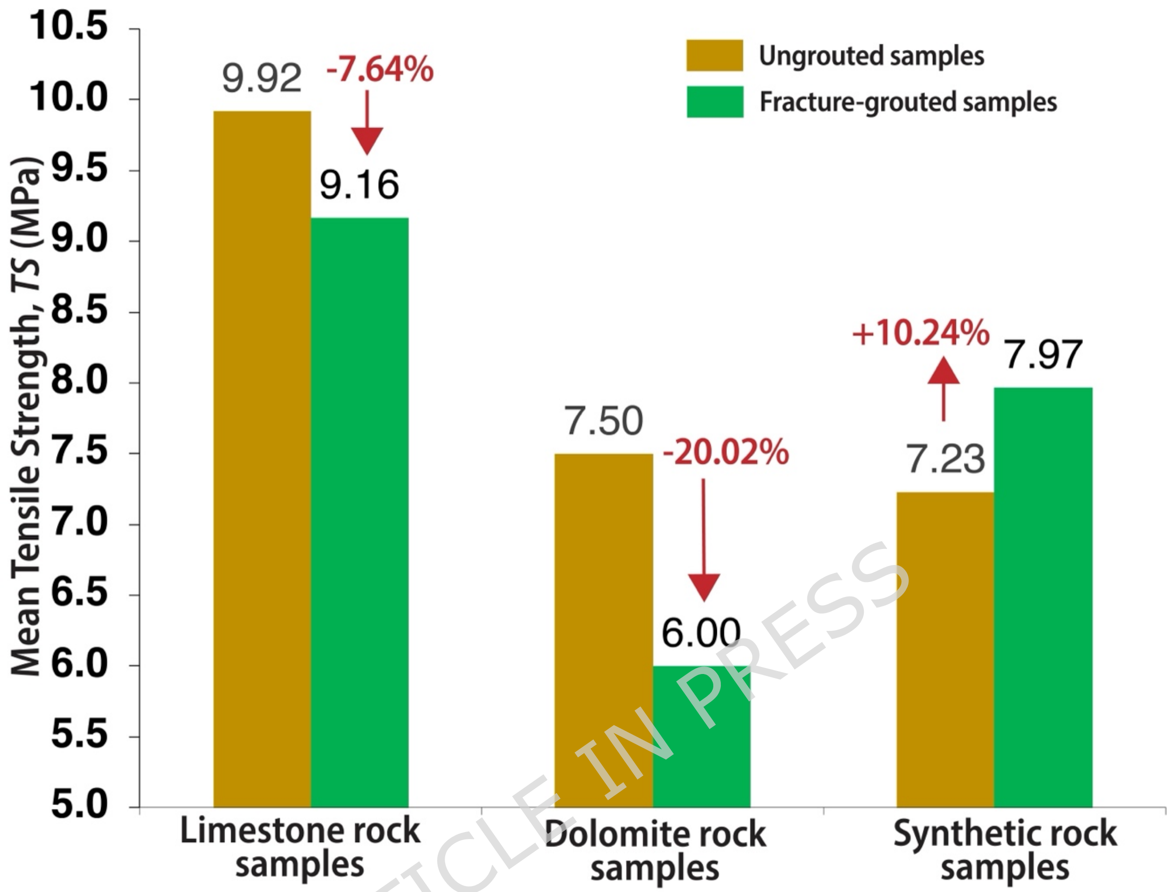

Figure 11: Analysis of mean tensile strength (*TS*) and percent changes for ungrouted and fracture-grouted rock samples across limestone, dolomite, and synthetic rock types.

The relatively superior performance of fracture-grouted limestone rock samples under tensile stress may reflect their generally tighter grain packing and lower inherent porosity compared to dolomite, characteristics that are documented in the literature for these lithologies (Gueguen & Palciauskas, 1994). These features may facilitate efficient stress distribution and limit microfracture initiation at fracture walls. Dolomite samples, by comparison, generally contain larger pore spaces and a more heterogeneous fabric at the fracture wall, which may promote microfracture nucleation and disjointed stress transfer. However, no direct microstructural characterization (such as CT scanning; scanning electron microscopy, SEM; or mercury intrusion porosimetry, MIP) was performed in this study, and these attributions therefore represent working hypotheses requiring further investigation with microstructural data.

Benchmarking against their ungrouted baselines, the mean *TS* of fracture-grouted natural rocks exhibited lower strength, with overall mean values of ~7.71 MPa compared to ~8.22 MPa for the same samples in their ungrouted condition (Tables 3 and 4; Fig. 11). Quantitatively, percentage changes in *TS* S of natural rocks post-grouting (Fig. 11) reveal a distinct trend where limestone rocks retained most of their tensile strength with a relatively small reduction of approximately 7.6% *TS* compared to inherent condition, whereas dolomite rocks yielded a more substantial decrease of approximately 20% *TS*. However, this should not be interpreted as a detrimental effect of rock fracture grouting. Rather, it reflects the fundamental difference in boundary conditions and rock material heterogeneity: fracture-grouted specimens behave as composite systems containing previously fractured planes under tensile stress, with new grout-rock interfaces and localized stiffness contrasts. The fracture-grouted natural rock samples exhibited reasonable resistance to tensile failure at stress levels close to the intact benchmarks (within ~6% *TS* on average), indicating partial tensile strength restoration and significant enhancement of structural integrity under tensile stress.

The synthetic rock samples present a contrasting behavior relative to natural rock samples, but were incorporated to examine the influence of intersecting fractures and smaller fracture aperture. Unlike fracture-grouted natural rock samples, fracture-grouted synthetic rock samples yielded higher *TS* than the ungrouted synthetic control (Fig. 11). This tensile response reversal is attributed to the inherently weaker base matrix of the 3D-printed material, which lacks the inter-granular mineralogical cohesion present in natural rocks such as limestone and dolomite. In such a weak matrix, grouting significantly improves tensile resistance by introducing new bonding interfaces and enhancing load transfer across fractures. This divergence between synthetic and natural rock responses has important engineering implications: the dominant mechanism of fracture-grouting reinforcement is rock-strength-dependent. In weak or poorly cemented rock masses (analogous to the 3D-printed material), grout injection can substantially increase apparent tensile strength beyond the base matrix, primarily acting as a strengthening agent. In competent natural rocks with strong intergranular cohesion, the grout-rock interface is inherently weaker than the original mineral bonding, so grouting cannot restore original tensile strength; instead, its dominant role shifts to fracture arrest and fracture-path control. This distinction, corroborated by the numerical simulation results showing a 38% reduction in fracture-tip stress concentration after grouting (Table 7), has direct implications for grouting strategy selection, which indicates that for weak, weathered, or fractured surrounding rock zones, the primary grouting benefit is strength enhancement, while for competent fractured rock, the relevant performance metric is fracture arrest and *TFL* reduction, not *TS* recovery to intact-rock levels.

However, when injected into underground surrounding rock fractures, grouts (slurry) act not only as a fracture filler but as a structural enhancement, compensating for the mechanical weakness in the rock mass. Thus, while there is lower *TS* in the synthetic samples, in underground natural rock masses with similar intersecting fractures, we envisage significant *TS* improvement after fracture grouting. Further, these *TS* reductions in fracture-grouted rocks relative to ungrouted conditions do not imply that grouting is ineffective. Rather, they reflect limitations in restoring pre-fracture strength when newly formed grout-rock interfaces are weaker than the original intergranular cohesion. The partial recovery of tensile strength in natural rock masses demonstrates the feasibility of fracture grouting to enhance mechanical performance, particularly in fractured or weak zones underground. These findings highlight that while grouting may not fully restore the inherent *TS* of natural rocks, it can substantially improve tensile strength and structural integrity by limiting fracture propagation and enhancing resistance to tensile failure. The benefits of grouting are especially pronounced in weaker and weathered underground rock masses with multiple fractures, suggesting that fracture-grouting treatment should be tailored to the specific mechanical and microstructural characteristics of the parent rock mass.

4.2 Micro-Fracture Propagation and Tensile-Induced Failure Modes

4.2.1 Insights from Experimental Observations

Following the Brazilian Disc Test (BDT), distinct fracture behavior was observed in natural rock samples (limestone and dolomite, Figs. 12-13) and synthetic rocks (Fig. 14) before and after grouting. In the natural rock samples, visible tensile-induced microfractures developed upon failure, often propagating along grain boundaries and pre-existing planes of weakness in both ungrouted and fracture-grouted conditions. In contrast, fracture-grouted synthetic samples exhibited latent failure and no observable fracturing when subjected to tensile stress, instead failing as cohesive bulk units. This divergence is attributed to the intrinsic material properties of the 3D-printed analogs, which possess a homogeneous internal structure and lack the mineralogical heterogeneity that facilitates fracture initiation and propagation in natural rocks. The uniformity of the synthetic materials suppresses localized stress concentrations, resulting in a more unified, latent failure response (Fig. 14). These observations indicate that synthetic (3D-printed) rocks may not serve as reliable analogs for observing fracture morphology in rock masses, while remaining useful for controlled strength studies.

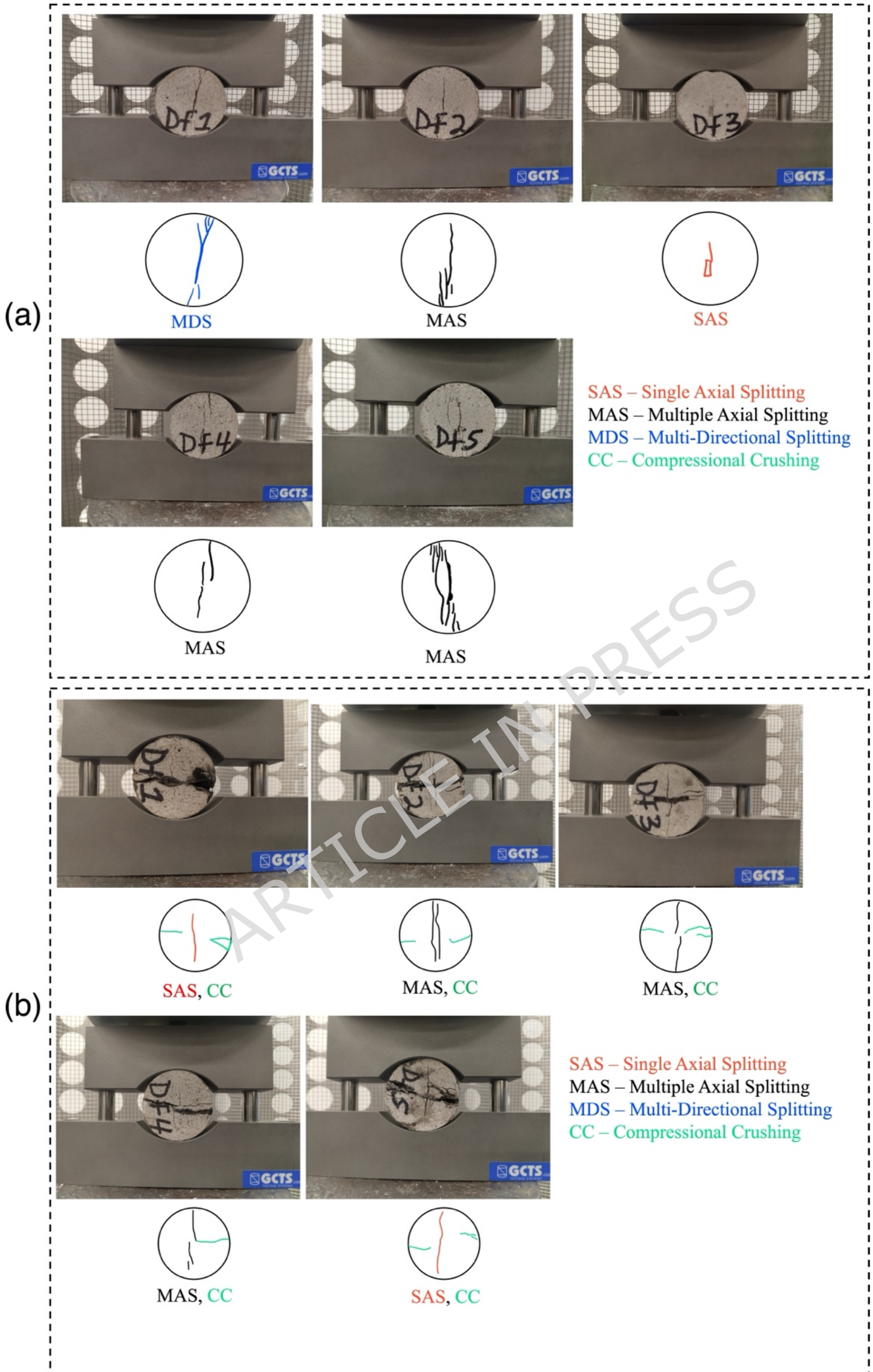

677
678 Figure 12: Failure modes in dolomite disc samples: (a) primary tensile-induced fracture patterns developed
679 in samples before grouting, and (b) secondary tensile-induced fracture patterns developed in samples after
680 fracture grouting. Colors indicate distinct tensile-induced failure modes.

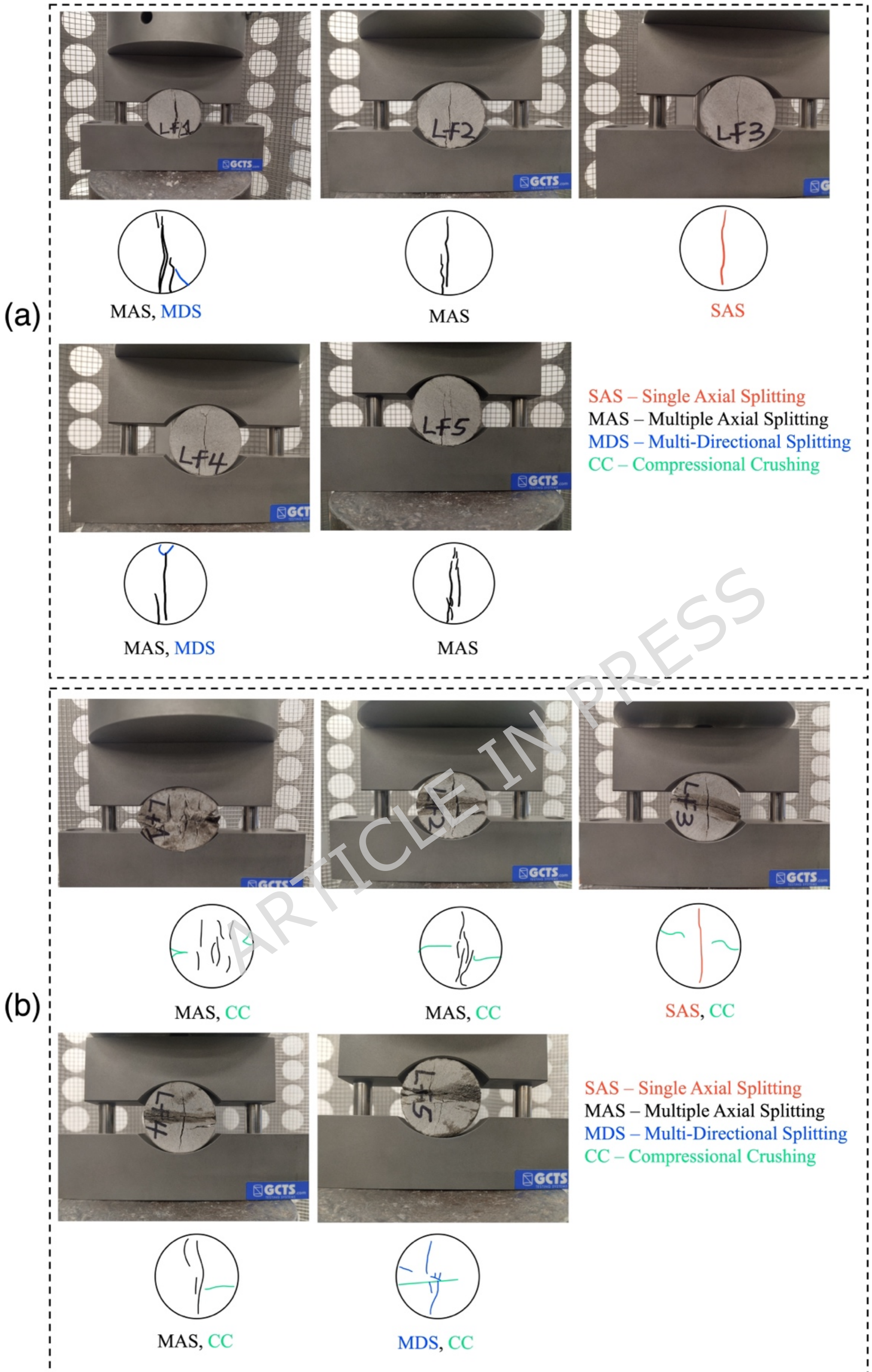

681

682 Figure 13: Failure modes in limestone disc samples: (a) primary tensile-induced fracture patterns developed
683 in samples before grouting, and (b) secondary tensile-induced fracture patterns developed in samples after
684 fracture grouting. Colors indicate distinct tensile-induced failure modes.

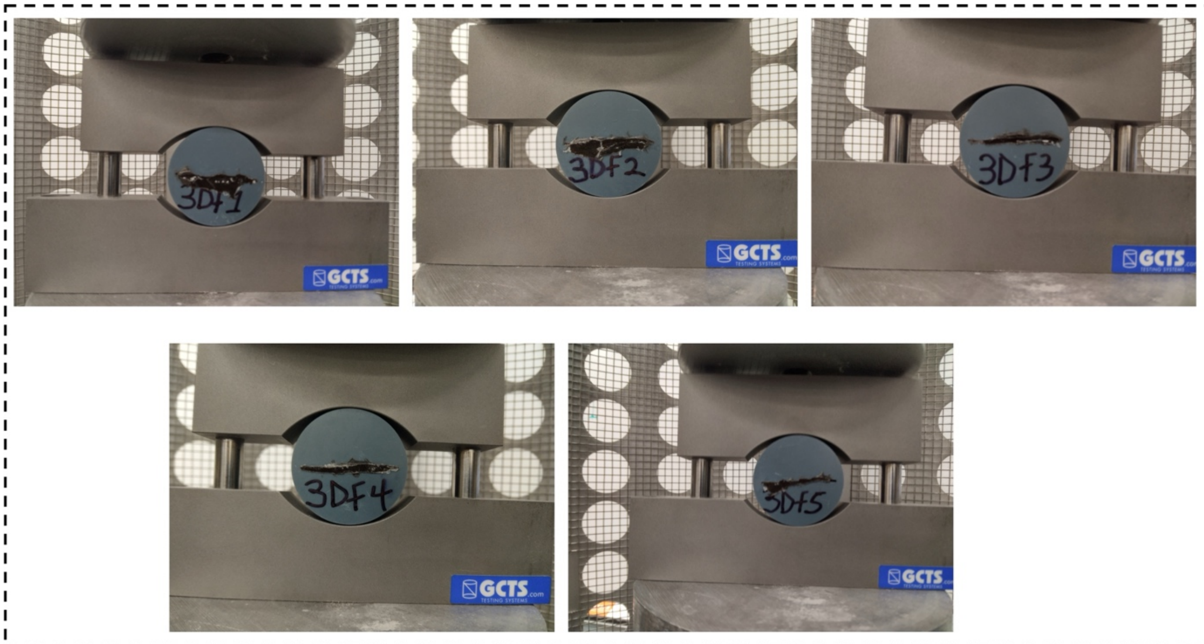

Figure 14: Latent tensile failure patterns in fracture-grouted synthetic (3D-printed) rock samples.

In the ungrouted and fracture-grouted natural rock disc samples, four (4) primary tensile-induced failure modes were identified: (a) single axial splitting (SAS) mode, (b) multiple axial splitting (MAS) mode, (c) multi-directional splitting (MDS) mode, and (d) compressional crushing (CC) mode. Understanding these tensile-induced rock failure modes provides critical insight into how grouting influences mechanical behavior and fracture evolution in tension-dominated underground environments.

The SAS mode is characterized by a fracture initiating at the center of the rock disc and propagating vertically along the loading axis. This is the most representative failure mode for true tensile strength under ideal BDT conditions (ASTM, 2023; Markides & Kourkoulis, 2024), indicating symmetric loading and minimal influence from anisotropy or boundary effects. Consistently achieving this idealized mode is challenging due to the inherent heterogeneity of natural rock masses: variations in mineral composition, microstructure, and pore distribution create local stress concentrations, while stronger mineral grains cause crack deflection. The MAS mode shares the same fundamental mechanics as SAS but involves more than one vertical coalesced fracture in the rock disc, arising from localized variations in mechanical properties such as grain size, mineralogy, or cementation, creating multiple zones of stress concentration. MAS is frequently observed in sedimentary rocks with layered or banded structures, where parallel fractures reflect anisotropic tensile response.

The MDS mode involves fracture propagation at various angles relative to the loading axis, resulting from a combination of tensile and shear stresses. This mixed-mode failure is typically associated with rock masses exhibiting complex internal structures, irregular bedding orientations, or intersecting discontinuities. MDS mode reflects a departure from ideal tensile failure and indicates that internal rock architecture significantly influences fracture trajectory. The CC mode is characterized by failure along planes perpendicular to the applied load, often at contact points between loading jaws and the disc sample. While BDT is designed to induce tensile failure, CC mode can occur when compressive stress dominates locally, particularly in zones of poor bonding or weak rock-grout interfaces. In this study, CC mode was observed primarily in fracture-grouted rock samples, where stress transmission across grout-filled fractures was less efficient due to imperfect bonding or stiffness mismatch, leading to stress localization and rupture along these planes of weakness.

Fig. 12-14 illustrates more specific primary or secondary tensile-induced failure modes observed across five representative disc samples of each rock type and condition studied. For ungrouted dolomite (Fig. 12a, MAS and MDS failure modes were both dominant, whereas for fracture-grouted dolomite (Fig. 12b), SAS and CC tensile-induced failure modes were most dominant, with short intruding lateral fracture propagation and increased mixed-mode energy dissipation. For ungrouted limestone (Fig. 13a), MAS was the dominant failure mode, with occasional MDS observed, whereas for fracture-grouted limestone (Fig. 13b), tensile-induced failure was marked by multiple axial fractures intersected by curved fracture paths. These patterns are consistent with the tensile behavior of layered sedimentary rock masses in an underground environment, where mechanical anisotropy and bedding plane influences fracture localization. The grout filling of the rock fractures appeared to have altered the stress distribution, and reinforced certain zones while introducing new interfaces that redirected fracture propagation.

4.2.2 Insights from Numerical Simulation

Fig. 15 shows the simulated fracture propagation sequences from damage initiation (at 50% Pp_{eak}) to complete failure (at 100% Pp_{eak}) for the aforementioned four simulation cases (Cases 1-4). In all cases simulated, fracture initiation occurred at or near the pre-existing fracture tips (or the grout-rock interface tips), consistent with stress concentration analysis and experimental observations.

For ungrouted limestone (Case 1), fracture propagation from the crack tips is predominantly Mode-I driven, and the simulation reproduces the experimentally dominant MAS failure mode, with an occasional MDS component (Fig. 15a). The simulated primary fracture path propagates vertically in the rock sample along the loading axis from both fracture tips toward the loading platens. A secondary axial crack, offset ~3.5 mm from the primary crack, initiates at ~85% of peak load (85% P_{peak}) and propagates in parallel, forming the characteristic MAS pattern of two or more subparallel vertical cracks. At ~90% of peak load (90% P_{peak}) and beyond, an oblique MDS crack nucleates from the upper and lower fracture tips at an angle of ~40° from horizontal, consistent with the occasional MDS failure mode observed experimentally. The Mode-I fracture energy dissipation accounted for 84% of total fracture energy, consistent with the tensile dominance of the MAS failure mode. The simulated primary fracture path length at failure was 29.7 mm, consistent with the experimental *TFL* range reported in Table 5.

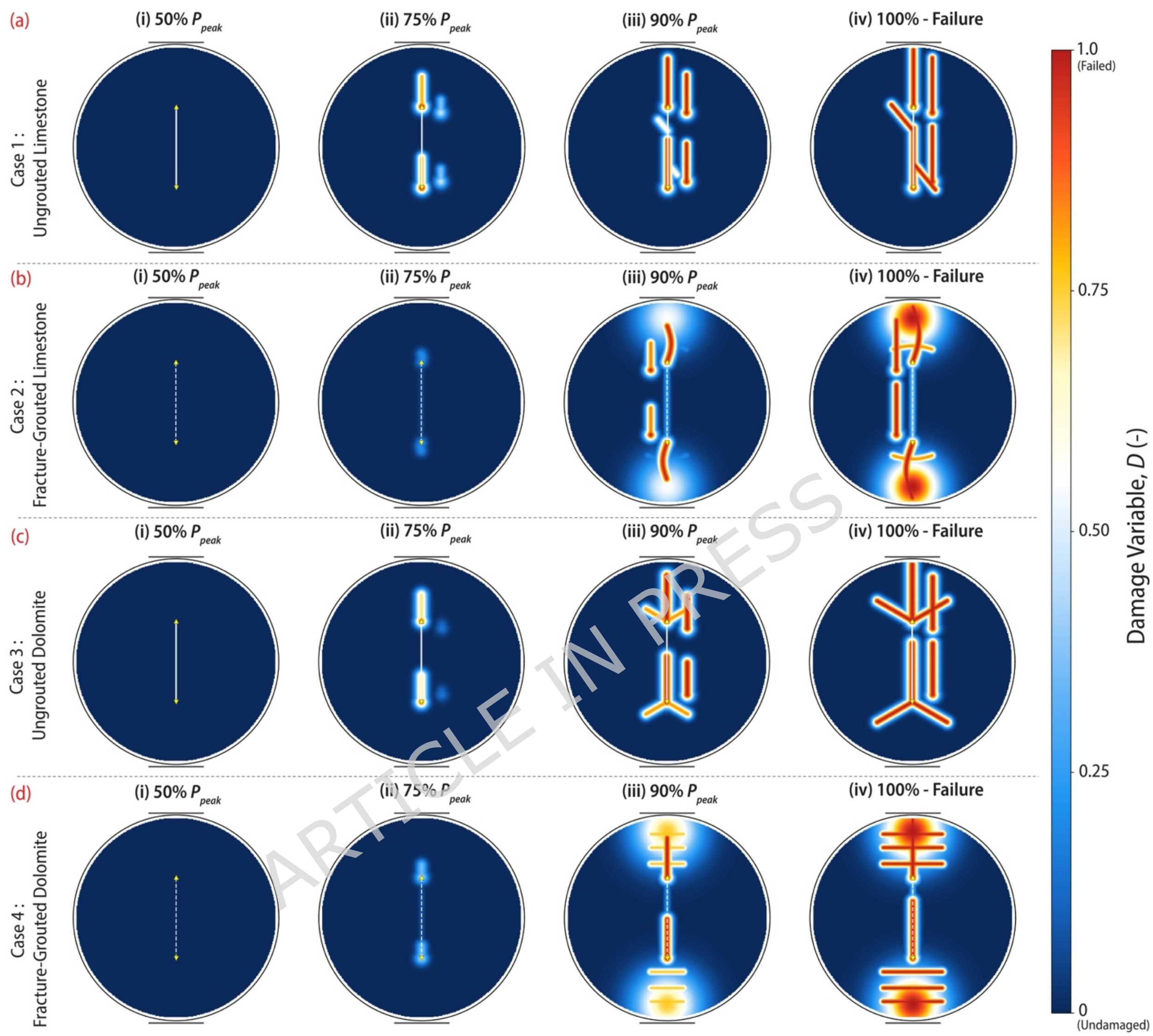

Figure 15: Simulated fracture propagation sequences (damage variable) from pre-initiation to complete failure for (a) ungrouted limestone [Case 1: MAS dominant, occasional MDS], (b) fracture-grouted limestone [Case 2: MAS intersected by curved CC paths], (c) ungrouted dolomite [Case 3: MAS and MDS dominant], and (d) fracture-grouted dolomite [Case 4: SAS and CC with short intruding lateral fractures]. [Yellow triangles mark the original fracture tips; white solid and dashed lines indicate the fracture interface for ungrouted and fracture-grouted specimens, respectively. Color scale: D = 0 (blue, undamaged) to D = 1 (red, fully failed)].

For fracture-grouted limestone (Case 2), the simulation reproduces the experimentally observed failure pattern of multiple axial fractures (MAS) intersected by curved fracture paths [CC mode] (Fig. 15b). The primary MAS crack propagates from both fracture tips with a sinuous lateral deviation, reflecting path redirection at the grout-rock interface. A second, parallel axial crack initiates at ~25% of loading progress beyond onset, preserving the multi-crack MAS character of the failure. From ~55% of loading (55% P_{peak}) progress onward, curved arc-shaped damage zones develop in the upper and lower halves of the rock disc and intersect the axial MAS cracks, consistent with the experimentally observed CC curved intersection paths. CC damage zones also developed prominently at the loading platen contact regions. The grout-rock interface sustains partial damage throughout the loading process, acting as a constraint that redirects the primary fracture path and introduces the curved CC intersection component. The Mode-II fracture energy dissipation fraction increases to 26% (from 16% in the ungrouted case), quantitatively consistent with the experimental observation of increased CC mode contribution after grouting. The simulated fracture path at failure (22.4 mm, a 25% reduction from the ungrouted case) is consistent with the experimental *TFL* reduction observed in Table 5.

For ungrouted dolomite (Case 3), the simulation is consistent with the experimentally dominant MAS combined with MDS failure pattern (Fig. 15c). Similar to limestone, the primary MAS component consists of a central axial crack and a secondary axial crack offset by ~3.8 mm, both propagating from the fracture tips. However, the MDS component is significantly more prominent in dolomite than in limestone (appearing at ~45% of loading progress beyond onset rather than 65%), consistent with the experimental observation that MDS is a dominant (rather than occasional) mode in dolomite. Four oblique MDS cracks radiate from the upper and lower fracture tips (two per tip, at approximately 30° and 150°), producing the characteristic multi-directional, radial-like fracture pattern observed experimentally. The wider fracture process zone in dolomite (reflecting the lower elastic modulus, E = 40 GPa vs. 46 GPa for limestone) produces a more diffuse damage distribution compared to the limestone cases. The Mode-I energy fraction remains 82% at failure, consistent with the combined MAS and MDS tensile character of the failure mode. The simulated primary fracture path length at failure was 27.1 mm, consistent with the experimental *TFL* range for ungrouted dolomite in Table 5. For fracture-grouted dolomite (Case 4), the simulation reproduces the experimentally dominant single axial splitting (SAS) combined with CC failure mode, with short intruding lateral fracture propagation and increased mixed-mode energy dissipation (Fig. 15d). This failure pattern is distinctly different from the other three cases. The damage field is dominated by a single central vertical through-crack (SAS), rather than the multiple parallel axial cracks of the MAS mode. From ~30% of loading progress beyond onset, short perpendicular lateral fractures branch off the primary SAS crack at regular intervals along its length, producing the characteristic intruding lateral fracture pattern observed experimentally. These lateral branches are relatively short (maximum ~5.5 mm), consistent with the experimental description of short-intruding lateral fracture propagation. Prominent CC damage zones develop at both loading platen contact regions. The Mode-II fracture energy dissipation fraction increases to 29% of total fracture energy for Case 4, the highest among all four cases, consistent with the experimentally observed increased mixed-mode energy dissipation in fracture-grouted dolomite. This increased mixed-mode character is attributed to the combined effect of the SAS crack interacting with lateral branches and the CC zones, generating local shear stress components along the fracture path. The simulated primary fracture path at failure (19.8 mm, a 27% reduction from ungrouted dolomite) is consistent with the experimental *TFL* reduction observed after grouting in Table 5. Furthermore, the simulated fracture paths in grouted specimens exhibit crack deflection and arrest at the grout-rock interface, resulting in shorter fracture path lengths at failure, consistent with the experimentally observed reduction in *TFL*. These findings confirm that the grout-rock interface acts as a fracture-arresting and path-redirecting medium, as hypothesized from the experimental *TFL* observations.

4.3 Relationship Between Tensile Strength (TS) and Total Fracture Length (TFL) of Fractured-Grouted Rocks: Experimental and Numerical Perspectives

Total Fracture Length (*TFL*) refers to the cumulative length of all visible fractures within a tested rock sample, measured individually and summed after failure, following the aforementioned protocol. This property was introduced as a comparative metric for rock tensile strength analyses by Khanlari et al. (2015). Fig. 16 presents the correlation between *TS* and *TFL* for natural (limestone and dolomite) rock disc samples across both fracture-grouted and ungrouted conditions. As no observable fractures were identified in synthetic rock samples following failure (Fig. 14), the subsequent analyses focus exclusively on natural rock samples. In the ungrouted rock samples (Fig. 16a), a positive correlation between *TS* and *TFL* is evident based on increasing trends of both *TS* and *TFL* in the same direction, suggesting that ungrouted rocks tend to exhibit more extensive fracture propagation under tensile loading. Mechanistically, this behavior can be attributed to the greater energy storage and release capacity of the rock fabric, which, upon reaching tensile failure, dissipates energy through the development of coalesced and more complex fracture networks. The FEM-CZM simulations corroborate this trend, showing that higher-strength ungrouted limestone (simulated *TS* = 9.79 MPa) produced a longer simulated fracture path (29.7 mm) than ungrouted dolomite (27.1 mm at simulated *TS* = 7.44 MPa; Table 7), consistent with the positive *TS*-*TFL* trend observed experimentally. This aligns with prior findings by Khanlari et al. (2015), where higher rock strength correlated with increased fracture extent due to more robust energy accumulation prior to rupture.

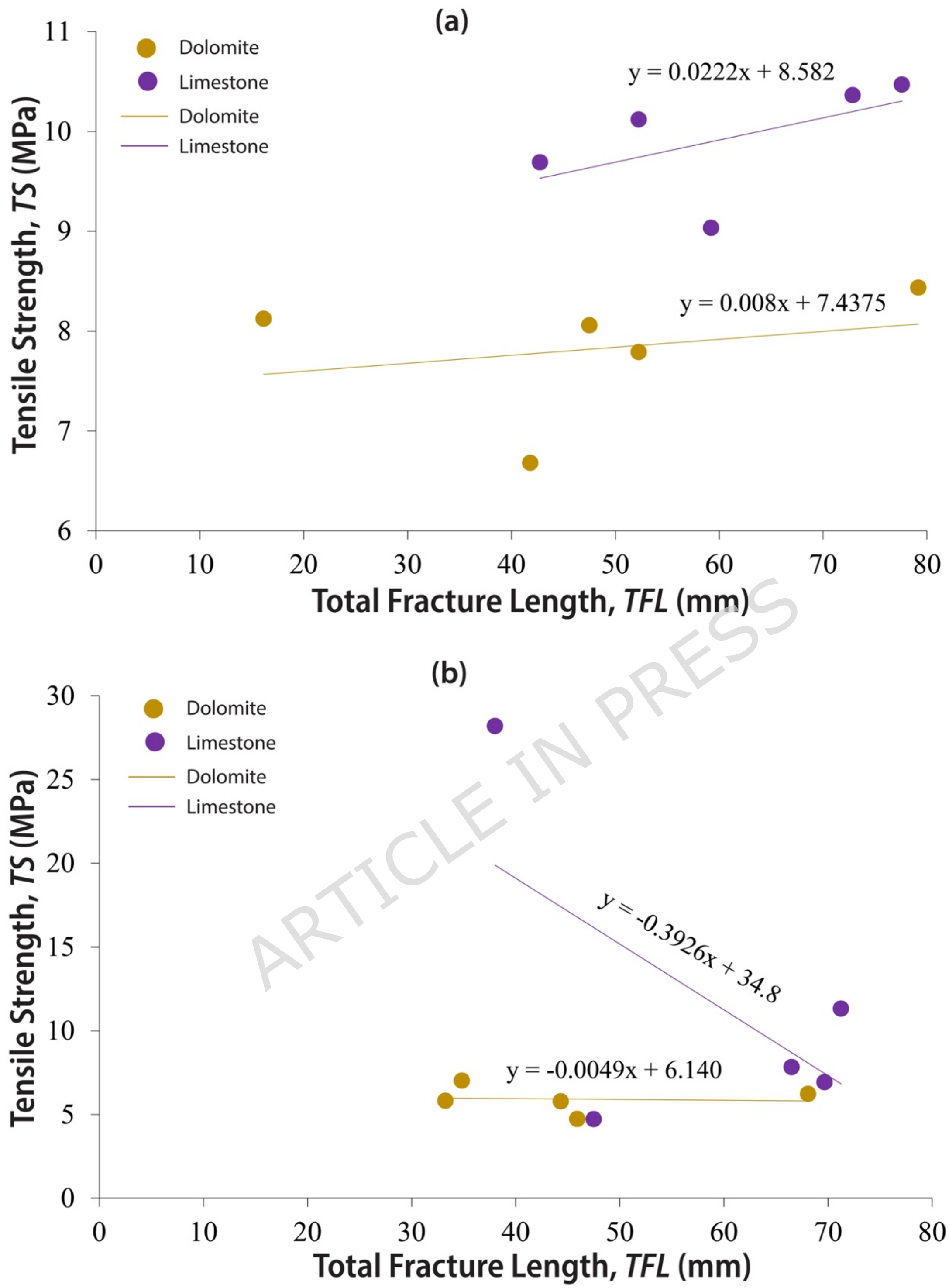

Figure 16: Correlation between Total Fracture Length (*TFL*) and tensile strength (*TS*) of limestone and dolomite rocks: (a) ungrouted rocks without grouting, and (b) fracture-grouted rock masses.

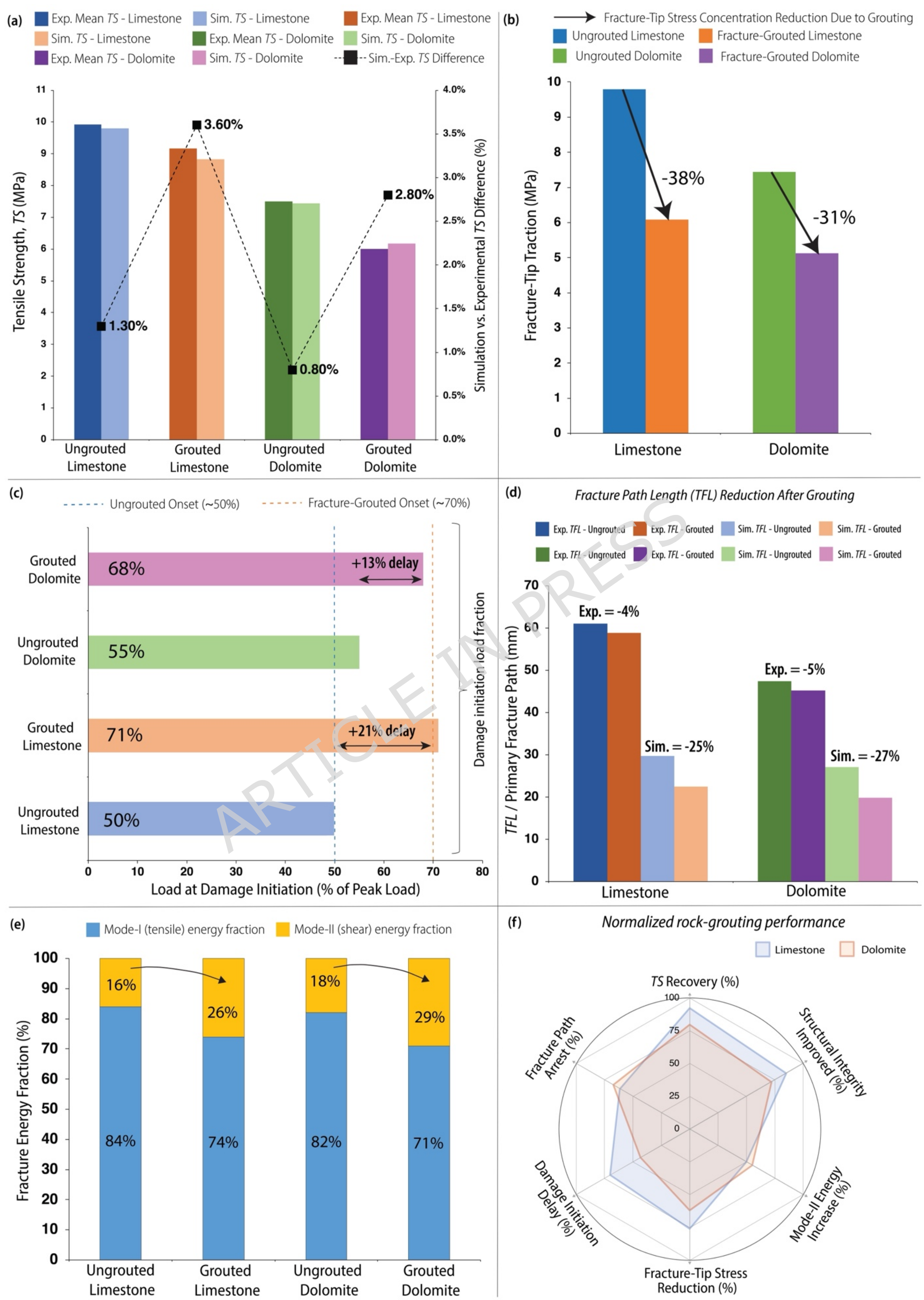
(a)
Exp. Mean TS - Limestone
Sim. TS - Limestone
Exp. Mean TS - Limestone
Sim. TS - Limestone
Exp. Mean TS - Dolomite
Sim. TS - Dolomite
Exp. Mean TS - Dolomite
Sim. TS - Dolomite
Sim.-Exp. TS Difference
Tensile Strength, TS (MPa)
Simulation vs. Experimental TS Difference (%)
1.30%
3.60%
0.80%
2.80%
Ungrouted Limestone
Grouted Limestone
Ungrouted Dolomite
Grouted Dolomite
(b)
Fracture-Tip Stress Concentration Reduction Due to Grouting
Ungrouted Limestone
Fracture-Grouted Limestone
Ungrouted Dolomite
Fracture-Grouted Dolomite
Fracture-Tip Traction (MPa)
-38%
-31%
Limestone
Dolomite
(c)
Ungrouted Onset (~50%)
Fracture-Grouted Onset (~70%)
Grouted Dolomite
68%
+13% delay
Ungrouted Dolomite
55%
Grouted Limestone
71%
+21% delay
Ungrouted Limestone
50%
Damage initiation load fraction
Load at Damage Initiation (% of Peak Load)
(d)
Fracture Path Length (TFL) Reduction After Grouting
Exp. TFL - Ungrouted
Exp. TFL - Grouted
Sim. TFL - Ungrouted
Sim. TFL - Grouted
TFL / Primary Fracture Path (mm)
Exp. = -4%
Sim. = -25%
Exp. = -5%
Sim. = -27%
Limestone
Dolomite
(e)
Mode-I (tensile) energy fraction
Mode-II (shear) energy fraction
Fracture Energy Fraction (%)
16%
84%
26%
74%
18%
82%
29%
71%
Ungrouted Limestone
Grouted Limestone
Ungrouted Dolomite
Grouted Dolomite
(f)
Normalized rock-grouting performance
Limestone
Dolomite
TS Recovery (%)
Structural Integrity Improved (%)
Mode-II Energy Increase (%)
Fracture-Tip Stress Reduction (%)
Damage Initiation Delay (%)
Fracture Path Arrest (%)

822

Figure 17: Quantitative analyses of FEM-CZM simulations validated experimental results in natural rocks (limestone and dolomite) in ungrouted and fracture-grouted conditions: (a) experimental vs. simulated *TS* recovery, (b) fracture-tip stress concentration reduction due to grouting (at 50% peak load), (c) damage initiation load fraction, (d) fracture path length (*TFL*) reduction after grouting, (e) Mode-I and Mode-II fracture energy dissipation fractions, and (f) normalized multi-metric rock-grouting performance radar chart.

Fracture-grouted samples (Fig. 16b) showed a contrasting, inverse relationship between *TS* and *TFL*, with rock samples with higher tensile strength tend to exhibit shorter total fracture lengths. This reversal is indicative of the altered fracture mechanical behavior introduced by grouting. The numerical simulations provide a mechanistic explanation for this reversal, indicating that in fracture-grouted specimens, the grout-rock interface acts as a fracture-arresting medium, redistributing stress and limiting the development of extensive fracture networks. Higher-stiffness grout distributions (producing higher grouted *TS*) are also more effective at deflecting and arresting fracture propagation, leading to shorter fracture paths. The simulated fracture-path reduction of 24-27% after grouting (Table 7) is quantitatively consistent with the experimentally observed reduction in *TFL*. The inverse *TS*-*TFL* relationship in grouted specimens is therefore a direct consequence of the fracture-arresting role of the grout-rock interface, as directly visualized in the simulation results.

Despite the overall lower *TS* values observed in fracture-grouted samples compared to ungrouted states, the reduction in *TFL* signifies an enhancement in mechanical response and structural integrity. The injected grout not only fills rock fractures but modifies the stress field, promoting deflection or termination of propagating fractures at grout-rock boundaries. This behavior highlights the importance of evaluating grouting performance not solely by peak rock strength recovery but by its ability to inhibit fracture propagation, which is critical in tension-dominated failure zones underground. The contrasting *TS*-*TFL* relationships between ungrouted and fracture-grouted rock samples highlight the influence of material heterogeneity and interfacial mechanics on fracture dynamics. In ungrouted rock samples, tensile strength and fracture extent are positively coupled due to uniform energy dissipation. In fracture-grouted rocks, the composite nature introduces barriers to fracture growth, resulting in shorter *TFL* even at relatively high tensile stresses.

Fig. 17 presents a consolidated quantitative comparison of FEM-CZM simulation outputs against experimental BDT results across all four specimen conditions, spanning six performance dimensions. The simulation-to-experiment agreement for tensile strength (Fig. 17a) is within 4% across all conditions, validating the FEM-CZM framework as a reliable predictor of BDT behavior for both lithologies and both grouting states. Fig. 17b-c together provide mechanistic quantifications of the fracture arrest role of grouting that is not accessible from experimental measurements alone, showing that grouting reduces fracture-tip stress concentrations by 31-38% and delays damage initiation to 68-71% of peak load (compared to 50-55% in ungrouted specimens), directly suppressing the stress intensification that drives progressive fracture development. The fracture path length comparison in Fig. 17d confirms that this delay in damage onset translates to a measurable reduction in fracture propagation extent, with simulated primary fracture paths reduced by 25-27% after grouting, consistent with the experimentally observed reductions in *TFL* reported in Table 5. The shift in Mode-II energy dissipation from 16-18% to 26-29% of total fracture energy after grouting (Fig. 17e) provides a quantitative basis for the experimentally observed transition from predominantly MAS mode to MAS combined with CC failure modes, confirming that the grout-rock interface introduces lateral fracture path deviations that redirect fracture energy and limit through-crack development. In a combined analysis, the radar chart (Fig. 17f) illustrates that limestone consistently outperforms dolomite across most grouting performance metrics, particularly in tensile strength retention and fracture path arrest, reflecting the differences in rock fabric and stiffness contrast at the grout-rock interface between the two lithologies, as previously observed in this study.

Fracture property analyses across all natural rock samples confirm that grouting curtailed post-failure fracture development. Compared with ungrouted conditions, fracture-grouted samples exhibited reduced *TFL* (shorter cumulative fracture paths at failure), indicating effective fracture arrest and deflection at grout-filled interfaces. This outcome converges with the observed shift in failure patterns, indicating that while ungrouted rocks frequently manifested MAS or MDS failure modes, fracture-grouted samples showed more constrained fracture networks and, in some cases, localized CC failure at contacts, consistent with stress redistribution across composite interfaces. These findings suggest that *TFL* may not serve as a reliable standalone indicator of higher tensile strength in fracture-grouted rocks or other rock–grout composite systems; however, *TFL* is proposed herein as a reliable performance metric for grouted surrounding rock masses under tensile stress when used alongside other complementary mechanical parameters (such as *TS*, failure mode, and simulated damage-path analysis). Ultimately, these results have direct implications for the design and assessment of grouting strategies for weak rock masses in underground to stabilize infrastructure. Specifically, it shows the need to consider not only rock tensile strength recovery to the inherent state but also fracture control as a key performance metric. By limiting fracture propagation, fracture grouting enhances the residual load-bearing capacity and mitigates the risk of progressive failure, particularly in underground zones susceptible to tensile stress concentrations.

5 Implications for Grout Reinforcement Strategy in Underground Surrounding Rock Masses

During underground excavation of tunnels, mines, wellbores, or caverns, the surrounding rocks often contain pronounced defects and discontinuities, particularly fractures, arising from both external disturbances and the inherent characteristics of the rock mass. These flaws reduce the mechanical integrity of surrounding rock masses and pose significant stability risks to underground infrastructure, particularly in areas where excavation-induced unloading, stress redistribution, and anisotropic rock deformation promote localized tensile stress concentrations. To reduce geological hazards and catastrophic failures in such projects, grouting, which is widely recognized as an effective reinforcement technique, is commonly used to fill these fractures, thereby restoring the inherent stability of the surrounding rock mass. Thus, in assessing the broader implications of fracture grouting on underground rock mass performance under tensile stress, a comparative analysis of average *TS* across all tested rock types [natural (limestone and dolomite) and synthetic rocks] is needed across both fracture-grouted and ungrouted (intact) conditions. As analyzed in Fig. 18, ungrouted rocks yielded an average *TS* of 8.22 MPa, while the same rock samples after fracture grouting exhibited a slightly lower average of 7.71 MPa, corresponding to a reduction of approximately 6.16% *TS* relative to the inherent rock tensile strength. This reduction reflects the non-full restoration of inherent tensile strength following underground grout treatment. However, as previously noted, this does not diminish the value of grouting as an underground reinforcement strategy. The post-grouting tensile strength, though lower than inherent strength, demonstrates the ability of grout to impede fracture propagation, enhance stress redistribution, and improve the residual integrity of weak or weathered rock masses.

This reduction in *TS* after fracture grouting reflects the non-restoration of the inherent tensile strength and integrity of the rock mass following underground grout treatment. However, as previously noted, this outcome is not a limitation to grouting performance or to diminish the value of grouting as an underground reinforcement strategy in enhancing rock integrity. On the contrary, the post-grouting tensile strength, though lower than the inherent strength, demonstrates the ability of grout to impede fracture propagation, enhance stress redistribution, and improve the residual integrity of weak or weathered rock masses. In addition, it underscores the nature of grouted rock systems, where previously rock fractured planes and grout–rock interfaces introduce mechanical heterogeneity and localized stiffness contrasts. These features inherently alter stress distribution and fracture mechanics, resulting in lower peak *TS* values compared to ungrouted rocks. Yet, the restored tensile strength in fracture-grouted rocks remains sufficiently high to resist tensile-induced failure and suppress fracture propagation, thereby enhancing the structural integrity of the underground rock mass.

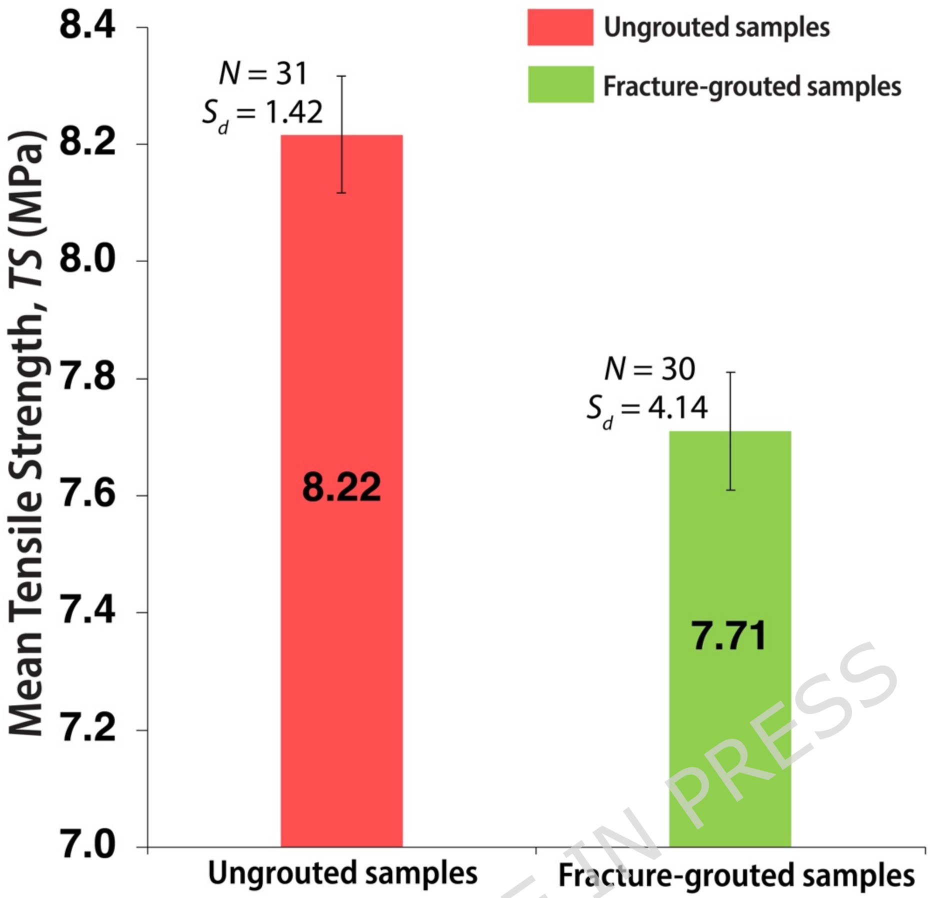

Figure 18: Analysis of mean tensile strength (*TS*) of underground rocks across distinct ungrouted and fracture-grouted conditions. S_d = Standard deviation, N = Number of samples.

The FEM-CZM numerical simulations provide additional mechanistic insight into the underground-engineering implications of fracture grouting. The simulations demonstrate that fracture grouting reduces fracture-tip stress concentrations by 31-38% and delays damage initiation to 68-71% of peak load (Table 7), directly reducing the risk of progressive fracture coalescence and unstable failure under tensile loading. While the simulated *TS* reductions after grouting (approximately 9-17%, Table 6) quantitatively reproduce the experimental observations, the simulated fracture path reductions of 25-27% provide direct quantitative evidence that grouting suppresses fracture propagation even when peak tensile strength is not fully recovered. These simulation results, combined with the experimental *TFL* analysis, confirm that fracture arrest and propagation control are the primary reinforcement mechanisms of grouting in tension-dominated surrounding rock.

The bonding provided by grout across rock fracture surfaces contributes not only to tensile failure resistance but may also introduce additional shear failure resistance, particularly in underground zones where both tensile and shear stresses interact (Wang et al., 2019; Liu et al., 2020; Hu et al., 2024; Yao et al., 2024). The numerical simulation results further reveal that grouting increases the mixed-mode character of fracture propagation (Mode-II energy fraction increasing from 16-18% to 26-29% after grouting, Table 7), consistent with the experimentally observed increase in CC failure mode. This dual reinforcement mechanism is critical in underground environments where complex stress fields arising from excavation-induced stress redistribution, anisotropic loading, and time-dependent deformation can promote tensile failure in bedrock. While grouting may not always fully recover the original *TS* of the rock mass, it can demonstrably improve residual mechanical integrity of fractured zones, reduce fracture coalescence, and delay failure onset.

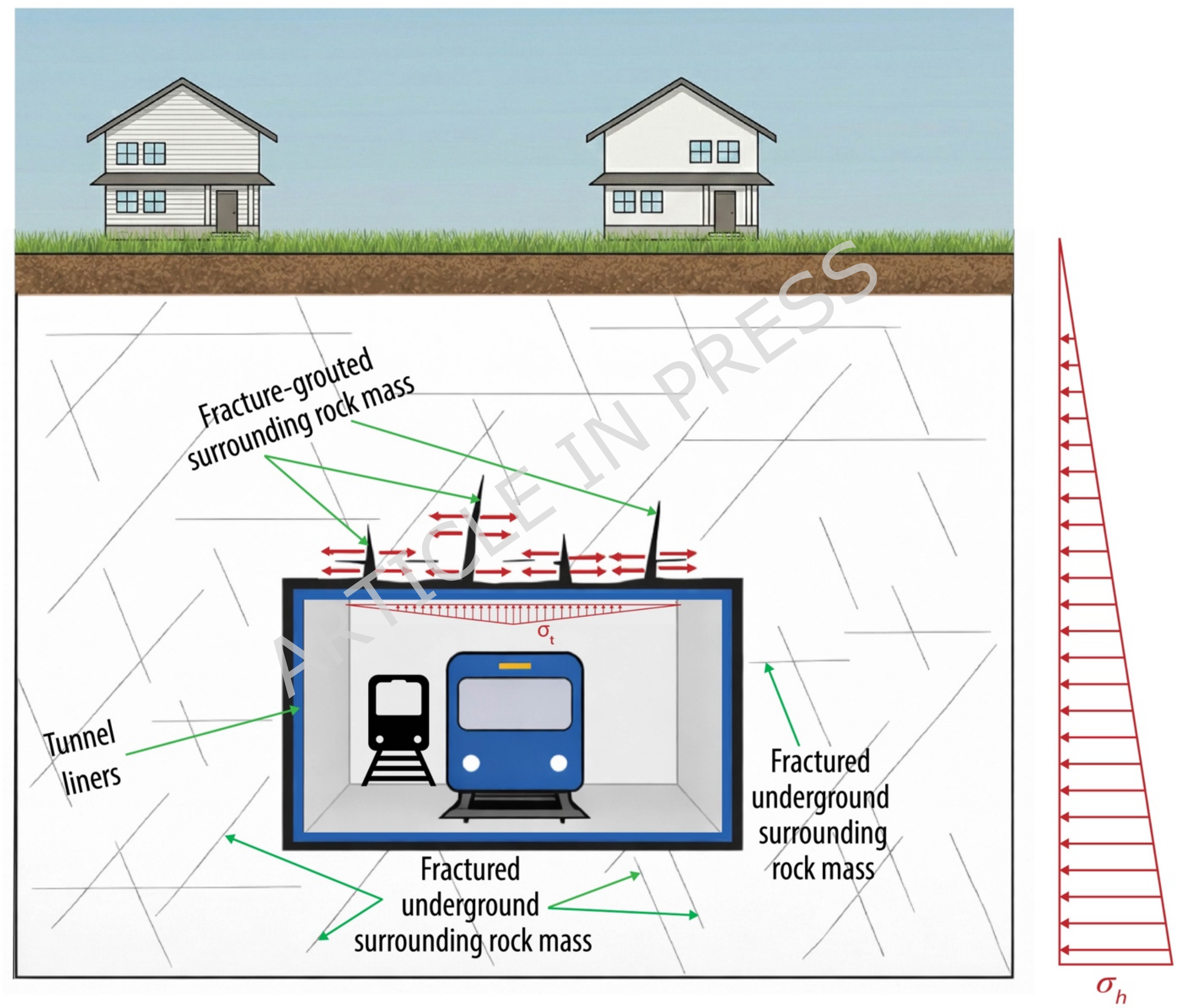

Figure 19: Illustration of fracture-grouted surrounding rock around an excavated underground opening (tunnel) and the tensile stress distribution around underground structures built on/within the rock mass.

The findings in this study suggest that grouting can serve as a less intrusive alternative to conventional support and reinforcement solutions in underground surrounding rock control (Fig. 19), particularly where traditional support systems such as rock bolts may be impractical or insufficient. The observed *TS* in fracture-grouted rocks indicates that grouting effectively enhanced the integrity of the rock mass under tensile loading, especially pronounced in weak or weathered bedrock zones, where grout can transform discontinuous rock fabrics into more cohesive systems capable of resisting tensile stresses. The use of advanced grouting materials with efficient dispersion potential, such as nanomagnetic slurries (Oppong & Kolawole, 2025; Sonibare et al., 2026), further amplifies this effect by improving penetration into small fracture apertures and enhancing interfacial bonding. The FEM-CZM framework developed in this study provides a validated numerical tool that can be extended to explore grout material optimization, fracture geometry effects, and in-situ stress conditions, supporting rational design of grouting strategies for underground infrastructure.

Although the aforementioned insights were highlighted in this study, limitations include: (a) microstructural data (CT scanning; scanning electron microscopy, SEM; or mercury intrusion porosimetry, MIP) were not collected, so attributions to rock porosity and fabric remain hypothetical; (b) sample fracture orientation relative to the loading axis was not systematically varied, and loadings were performed on specific fracture orientations; (c) only one grout type (nanomagnetic slurry) was tested; and (d) the study was conducted at laboratory scale with relatively small sample counts. Future investigations should explore the interplay between fracture orientation and size, grout types (including polymer-based and hybrid nanomaterial grouts), injection pressure and rate, grout placement, loading direction, and lithologic variability on tensile strength and behavior. Direct microstructural characterization of grout-rock interfaces would clarify mechanisms attributed to porosity and grain characteristics. Additionally, a three-group comparison design comprising (a) intact BDT, (b) BDT on refractured specimens at 90° without grouting, and (c) BDT on grouted specimens at 90°, should be incorporated in future studies to isolate the grouting contribution from directional effects. Despite these limitations, the findings provide significant contributions advancing understanding of rock mass grouting as a tensile strength reinforcement and fracture-development control strategy in underground rock masses.

Further, from an underground rock engineering design perspective, the results in this study emphasize that grouting should be evaluated for its ability to impede tensile fracture growth and stabilize fracture processes, not solely by the degree to which it restores inherent tensile strength (*TS*). In underground tension-dominated zones (e.g., excavation perimeters, roofs, and abutments), limiting fracture propagation can reduce the likelihood of coalescence into kinematically admissible blocks and mitigate slabby spall and roof fall. The observed changes in tensile strength (*TS*) indicate enhanced resistance to tensile failure and improved residual load-carrying capacity of the rock mass. Practically, this implies that grout selection and injection protocols should prioritize effective penetration and bonding across critical rock mass discontinuities to maximize fracture arrest, with performance verified through appropriate mechanical testing. Variations in *TFL* may also provide insight into the stress state and damage evolution of underground rock masses when quantified using imaging-based fracture analysis. In addition, reinforcement layouts should be designed with consideration of rock anisotropy and defect orientation to ensure optimal structural performance. Collectively, these insights support rock fracture grouting as a viable strategy for mitigating tension-related failure in underground infrastructure, even when the intrinsic tensile strength of rock mass is not fully restored.

6 Conclusions

This study investigated the evolution of tensile strength (*TS*) and tensile-induced fracture behavior of fractured surrounding rock before and after fracture grouting, to understand how grouting contributes to mechanical integrity in tension-dominated underground environments. Brazilian disc tests were conducted on natural (limestone and dolomite) and synthetic (3D-printed) rock disc samples in both ungrouted and fracture-grouted states. A new FEM-CZM numerical simulation framework was developed to mechanistically interpret and extend the experimental observations. Based on the experimental results, analyses, and numerical simulation, the following conclusions are drawn:

a. For natural rocks containing larger fracture aperture, fracture-grouted specimens exhibited tensile strengths lower than their ungrouted baselines, with TS reductions of approximately 7.6% for limestone and 20.2% for dolomite. The FEM-CZM simulations reproduced these reductions with less than 4% error and attributed them to the lower mechanical stiffness and strength of the grout-rock interface compared to the original intergranular cohesion.

b. Grouting treatment altered tensile failure mechanisms and fracture evolution in a lithology-dependent manner. Four distinct tensile-induced failure modes were identified across the four experimental conditions: MAS dominant with occasional MDS for ungrouted limestone, MAS intersected by curved CC paths for fracture-grouted limestone, co-dominant MAS and MDS for ungrouted dolomite, and SAS combined with CC and short intruding lateral fractures for fracture-grouted dolomite. The FEM-CZM numerical simulations directly confirmed all four failure mode patterns and quantified the associated Mode-I and Mode-II fracture energy fractions (Mode-I: 84%, 74%, 82%, and 71% for Cases 1-4, respectively), confirming that grouting consistently increases mixed-mode energy dissipation and that the degree of this increase is governed by the rock elastic modulus and the grout-rock stiffness contrast.

c. *TFL* revealed a distinct grouting-controlled fracture response. In ungrouted natural rocks, a positive correlation between *T*S and *TFL* was observed, reflecting greater energy dissipation in stronger rocks; and in contrast, fracture-grouted samples exhibited an inverse *TS*-*TFL* relationship. The FEM-CZM simulations confirmed this reversal mechanistically, showing that the grout-rock interface acts as a fracture-arresting medium that reduces the primary fracture path length by 25-

27% and reduces fracture-tip stress concentrations by 31-38%, even when peak tensile strength is not fully recovered.

d. The FEM-CZM numerical simulations demonstrate that fracture grouting delays crack initiation to 68-71% of peak load (compared to 50-55% in ungrouted specimens), providing a critical additional quantitative insight into the fracture arrest mechanism that was inaccessible from the experimental measurements alone. This delay in rock damage onset, combined with the observed fracture path reduction and Mode-II energy increase, provides a comprehensive mechanistic explanation for the experimentally observed improvement in structural integrity after grouting.

e. *TFL* is a valuable fracture-control metric when used alongside other rock mechanical parameters. While *TFL* alone is not a reliable indicator of tensile strength in fracture-grouted geosystems, its combined use with tensile strength, failure mode analysis, and numerical simulation-based damage assessment provides a comprehensive evaluation of grouting performance.

f. Rock type and heterogeneity majorly influenced fracture grouting effectiveness, with fractured limestone exhibiting better tensile strength retention after grouting than fractured dolomite, attributable to documented differences in rock fabric characteristics for these lithologies, though direct microstructural evidence was not collected in this study. Synthetic rock samples showed a contrasting response, confirming that synthetic analogs may not fully replicate the fracture behavior of heterogeneous natural rocks.

g. Although fracture grouting did not fully restore the inherent tensile strength of rock masses, it can significantly improve the mechanical integrity of fractured surrounding rocks by limiting fracture propagation and damage accumulation. Fracture-grouted rock samples retained tensile strengths (Mean *TS* approximately 7.7 MPa) close to inherent conditions (Mean *TS* approximately 8.2 MPa) and demonstrated improved resistance to tensile deformation.

This study provides mechanistic insight into how fracture grouting modifies tensile failure behavior in discontinuous rock masses. By integrating tensile strength measurements with fracture morphology, failure mode analysis, *TFL*, and FEM-CZM numerical simulation, this work demonstrates that grouting is an effective surrounding rock control strategy in tension-prone underground environments. The validated FEM-CZM numerical framework provides a powerful tool for future optimization of grouting strategies. Future work should incorporate fracture orientation, bedding anisotropy, grout rheology, varied injection rates, grout-rock interfacial mechanics, and direct microstructural characterization, as well as 3D numerical simulations with heterogeneous rock fabric and multiple fracture networks, field-scale validation through in-situ testing and monitoring, and the three-group BDT comparison to isolate the grouting contribution from directional loading effects.

Acknowledgment

We acknowledge the current and former members of the NJIT Geomechanics for Geo-Engineering and Sustainability (GGES) Lab for helping with laboratory measurements for this study.

Funding Declaration

This work was partially supported by a U.S. National Science Foundation (NSF) Accelerating Research Translation cooperative agreement (TIP-2331429) and the New Jersey Institute of Technology (NJIT) Center for Translational Research. The opinions, findings, and conclusions, or recommendations expressed are those of the author(s) and do not necessarily reflect the views of the National Science Foundation. This work was also supported by the Faculty Development and Research Internal Grant awarded by Newark College of Engineering, New Jersey Institute of Technology (NJIT).

Data Availability

The data analyzed in this study are available from the corresponding author upon request.

Authors Contribution Statement

O.K.: Conceptualization, Methodology, Formal analysis, Writing—original draft, Writing—review & editing, Supervision, Validation, Project administration, Visualization, Resources. M.O.S.: Writing—original draft. O.O.: Resources, Validation.

Declarations

Competing Interest: The authors declare no competing interests.

Consent for publication: The authors thoroughly reviewed the manuscript before submission and provided their consent for its publication.

References

Abdi, Y. (2024). Investigation of the strength behavior and failure modes of layered sedimentary rocks under Brazilian test conditions. *International Journal of Geo-Engineering*, *15*(1). https://doi.org/10.1186/s40703-024-00208-2.

ABAQUS. (2021). ABAQUS 6.14 Documentation. Dassault Systèmes Simulia Corp., Johnston, RI, USA. Accessed: May 11, 2026. http://62.108.178.35:2080/v6.14/books/usi/default.htm

ABAQUS. (2026). ABAQUS SIMULIA. Dassault Systèmes Simulia Corp., Johnston, RI, USA. Accessed: May 11, 2026. https://www.3ds.com/products/simulia/abaqus

Alcalde-Gonzalo, J., Prendes-Gero, M., Álvarez-Fernández, M., Álvarez-Vigil, A., & González-Nicieza, C. (2013). Roof tensile failures in underground excavations. *International Journal of Rock Mechanics and Mining Sciences*, *58*, 141–148. https://doi.org/10.1016/j.ijrmms.2012.10.003

Alejano, L. R. (2024). Rock mass Classification Systems: A useful rock mechanics tool, often misused. *Rock Mechanics and Rock Engineering*, *58*(10), 11147–11167. https://doi.org/10.1007/s00603-024-04087-y.

Asadizadeh, M., Khosravi, S., Abbasssalimi, N., Babanouri, N., Rezaei, M., Alipour, A., Lapcevic, V., Hedayat, A., & Sherizadeh, T. (2025). The effect of loading contact angle on the tensile behavior of rock disks. Rock Mechanics Letters, 2(3), 176-184. https://doi.org/10.70425/rml.202503.23

Askaripour, M., Saeidi, A., Rouleau, A., & Mercier-Langevin, P. (2022). Rockburst in underground excavations: A review of mechanism, classification, and prediction methods. *Underground Space*, *7*(4), 577–607. https://doi.org/10.1016/j.undsp.2021.11.008.

ASTM (2023) Standard Test Method for Splitting Tensile Strength of Intact Rock Core Specimens with Flat Loading platens. D3967-23: ASTM International, West Conshohocken, USA.

Baker, R., Senior. (1981). Tensile strength, tension cracks, and stability of slopes. *Soils and foundations*, *21*(2), 1–17. https://doi.org/10.3208/sandf1972.21.2_1

Barton, N., Lien, R., & Lunde, J. (1974). Engineering classification of rock masses for the design of tunnel support. *Rock Mechanics and Rock Engineering*, *6*(4), 189–236. https://doi.org/10.1007/bf01239496

Bell, F. G. (Ed.). (2013). *Engineering in rock masses*. Elsevier.

Bi, R., Liu, M., Zhou, J., & Du, K. (2025). Biaxial compression behavior and stability analysis of wedge blocks in tunnel sidewalls: Experimental investigation and support effect evaluation. *Underground Space*, *25*, 239–261. https://doi.org/10.1016/j.undsp.2025.05.008.

Bian, W., He, X., Wang, K., Wu, Y., Wang, G., Zhang, S., & Yang, J. (2026). Modeling and experimental validation of bolt–grout bond–slip behavior for deep underground excavation support. *Deep Underground Science and Engineering*. https://doi.org/10.1002/dug2.70074.

Bieniawski, Z.T. (1973). Engineering classification of jointed rock masses. Transactions of the South African Institution of Civil Engineers, 15(12), 335–344.

Bieniawski, Z.T. (1993). Classification of rock masses for engineering: The RMR system and future trends, In: Hudson, J.A., ed., Comprehensive Rock Engineering, Volume 3: Oxford; New York, Pergamon Press, p. 553-573.

Cai, M. (2007). Influence of intermediate principal stress on rock fracturing and strength near excavation boundaries—Insight from numerical modeling. *International Journal of Rock Mechanics and Mining Sciences*, *45*(5), 763–772. https://doi.org/10.1016/j.ijrmms.2007.07.026

Cai, M., & Kaiser, P. K. (2013). In-situ Rock Spalling Strength near Excavation Boundaries. *Rock Mechanics and Rock Engineering*, *47*(2), 659–675. https://doi.org/10.1007/s00603-013-0437-0

Cai, X., Yuan, J., Zhou, Z., Pi, Z., Tan, L., Wang, P., Wang, S., Wang, S., Wang, S., & Wang, S. (2023). Effects of hole shape on mechanical behavior and fracturing mechanism of rock: Implications for instability of underground openings. *Tunnelling and Underground Space Technology*, *141*, 105361. https://doi.org/10.1016/j.tust.2023.105361

Carter, B. J., Lajtai, E. Z., & Yuan, Y. (1992). Tensile fracture from circular cavities loaded in compression. *International Journal of Fracture*, *57*(3), 221–236. https://doi.org/10.1007/bf00035074

Chen, Z., Li, X., Dusseault, M. B., & Weng, L. (2020). Effect of excavation stress condition on hydraulic fracture behaviour. *Engineering Fracture Mechanics*, *226*, 106871. https://doi.org/10.1016/j.engfracmech.2020.106871

Cook, N.G.W. et al. (1966). Rock Mechanics applied to Rockbursts – a synthesis of the results of rockburst research in South Africa up to 1965. J. S. African Inst. Min. Metall. Vol. 66, No. 10, 435-528.

Diederichs, & Kaiser, P. (1999). Tensile strength and abutment relaxation as failure control mechanisms in underground excavations. *International Journal of Rock Mechanics and Mining Sciences*, *36*(1), 69–96. https://doi.org/10.1016/s0148-9062(98)00179-x

Du, Y., Du, X., Han, W., Wang, X., Huang, B., & Zhang, S. (2021). Fracture Behavior of Brazilian Disc Specimens Containing Fissure-Holes Based on the FEM-CZM Method. Geotech. Geol. Eng., 43, 92. https://doi.org/10.1007/s10706-024-03059-x

Goel, R. K., & Singh, B. (2011). *Engineering rock mass classification: tunnelling, foundations and landslides*. Elsevier.

Gueguen, Y., & Palciauskas, V. (1994). Introduction to the Physics of Rocks. 294 pp. Princeton: Princeton University Press. 1996;133(2):220-220. doi:10.1017/S0016756800008761.

Haeri, H., Shahriar, K., Marji, M. F., & Moarefvand, P. (2014). Experimental and numerical study of crack propagation and coalescence in pre-cracked rock-like disks. *International Journal of Rock Mechanics and Mining Sciences*, *67*, 20–28. https://doi.org/10.1016/j.ijrmms.2014.01.008.

Han, W., Jiang, Y., Luan, H., Du, Y., Zhu, Y., & Liu, J. (2020b). Numerical investigation on the shear behavior of rock-like materials containing fissure-holes with FEM-CZM method. Computers and Geotechnics, 125, 103670.

Han, W., Jiang, Y., Luan, H., Liu, J., Wu, X., & Du, Y. (2020a). Fracture evolution and failure mechanism of rock-like materials containing cross-flaws under the shearing effect. Theoretical and Applied Fracture Mechanics, 110, 102815. https://doi.org/10.1016/j.tafmec.2020.102815

Heidarzadeh, M., Tappin, D. R., & Ishibe, T. (2019). Modeling the large runup along a narrow segment of the Kaikoura coast, New Zealand following the November 2016 tsunami from a potential landslide. *Ocean Engineering*, *175*, 113–121. https://doi.org/10.1016/j.oceaneng.2019.02.024

Hoek, E. (1994). Strength of rock and rock masses. News J ISRM 2(2):4–16.

Hong, Z., Chen, S., Liu, X., & Li, F. (2024). Experimental study on mechanical properties of 3D Printed layered rock like materials. Scientific Reports, 14(1), 25367. https://doi.org/10.1038/s41598-024-77055-9

Hou, D., Zheng, X., Zhou, Y., Gong, C., & Wang, C. (2022). Analysis and application of surrounding rock mechanical parameters of jointed rock tunnel based on digital photography. *Geotechnical and Geological Engineering*, *41*(2), 721–739. https://doi.org/10.1007/s10706-022-02298-0

Hu, Q., Chen, G., Sun, X., Li, Y., & Liu, G. (2024). Effect of grouting on damage and fracture characteristics of fractured rocks under mode I loading. *Construction and Building Materials*, *418*, 135376. https://doi.org/10.1016/j.conbuildmat.2024.135376.

Hudson, J., Harrison, J., & Popescu, M. (2002). Engineering Rock Mechanics: An Introduction to the principles. *Applied Mechanics Reviews*, *55*(2), B30. https://doi.org/10.1115/1.1451165.

ISRM. (1978). Suggested methods for determining tensile strength of rock materials. *International* Journal of Rock Mechanics and Mining Sciences & Geomechanics Abstracts, 15(3), 99–103. https://doi.org/10.1016/0148-9062(78)90003-7.

Jiang, C., & Zhao, G.-F. (2015). A Preliminary Study of 3D Printing on Rock Mechanics. Rock Mechanics and Rock Engineering, 48(3), 1041–1050. https://doi.org/10.1007/s00603-014-0612-y

Jiang, J., Feng, X., Yang, C., & Su, G. (2020). Failure characteristics of surrounding rocks along the radial direction of underground excavations: An experimental study. *Engineering Geology*, *281*, 105984. https://doi.org/10.1016/j.enggeo.2020.105984.

Jing, S., Alves, T. M., Omosanya, K. O., & Li, W. (2023). Long-term slope instability induced by the reactivation of mass transport complexes: An underestimated geohazard on the Norwegian continental margin. *Geological Society of America Bulletin*. https://doi.org/10.1130/b36816.1

Jinpeng, Zhang, Liu Limin, and Li Yang. 2023. "Mechanism and Experiment of Self-Stress Grouting Reinforcement for Fractured Rock Mass of Underground Engineering." *Tunnelling and Underground Space Technology* 131:104826. doi:10.1016/j.tust.2022.104826.

Khanlari, G. R., Naseri, F., & Freire-Lista, D. M. (2019). Estimating compressive and flexural strength of travertines with respect to laminae-orientation by geomechanical properties. *Bulletin of Engineering Geology and the Environment*, *78*(3), 1451–1470. https://doi.org/10.1007/s10064-017-1139-8.

Khanlari, G., Rafiei, B., & Abdilor, Y. (2015). An Experimental Investigation of the Brazilian Tensile Strength and Failure Patterns of Laminated Sandstones. *Rock Mechanics and Rock Engineering*, 48(2), 843–852. https://doi.org/10.1007/s00603-014-0576-y.

Lei, Q., Latham, J., Xiang, J., & Tsang, C. (2017). Role of natural fractures in damage evolution around tunnel excavation in fractured rocks. *Engineering Geology*, *231*, 100–113. https://doi.org/10.1016/j.enggeo.2017.10.013

Li, D., & Wong, L. N. Y. (2013). The Brazilian Disc Test for Rock Mechanics Applications: Review and new insights. *Rock Mechanics and Rock Engineering*, *46*(2), 269–287. https://doi.org/10.1007/s00603-012-0257-7.

Li, P., Tang, C., Zhang, J., Guo, Q., Liu, Y., Wu, X., Cai, M., & Wang, Z. (2025). Mechanical properties and failure characteristics of pre-damaged fractured rocks under uniaxial compression. *Theoretical and Applied Fracture Mechanics*, *141*, 105305. https://doi.org/10.1016/j.tafmec.2025.105305

Li, T., Ma, C., Zhu, M., Meng, L., & Chen, G. (2017). Geomechanical types and mechanical analyses of rockbursts. *Engineering Geology*, *222*, 72–83. https://doi.org/10.1016/j.enggeo.2017.03.011.

Liao, J. J., Yang, M., & Hsieh, H. (1997). Direct tensile behavior of a transversely isotropic rock. *International Journal of Rock Mechanics and Mining Sciences*, *34*(5), 837–849. https://doi.org/10.1016/s1365-1609(96)00065-4

Liu, B., Sang, H., Wang, Z., & Kang, Y. (2020). Experimental Study on the Mechanical Properties of Rock Fracture after Grouting Reinforcement. *Energies*, *13*(18), 4814. https://doi.org/10.3390/en13184814

Liu, C. H., & Li, Y. Z. (2017). Analytical study of the mechanical behavior of fully grouted bolts in bedding rock slopes. *Rock Mechanics and Rock Engineering*, *50*(9), 2413–2423. https://doi.org/10.1007/s00603-017-1244-9

Liu, X., Liu, W., Zhang, G., Meng, Y., & Yin, Q. (2025). Studying the tensile mechanical behavior of soft-hard interlayer rock with experimental observation and FEM-CZM method. KSCE Journal of Civil Engineering, 29(5), 100099. https://doi.org/10.1016/j.kscej.2024.100099

Ma, S., & Ma, D. (2021). Grouting material for broken surrounding rock and its mechanical properties of grouting reinforcement. *Geotechnical and Geological Engineering*, *39*(5), 3785-3793.

Markides, C. F., & Kourkoulis, S. K. (2024). Reconsidering the determination of the tensile strength of orthotropic rocks by means of the Brazilian Disc Test. *Rock Mechanics and Rock Engineering*. https://doi.org/10.1007/s00603-024-04076-1

Martino, J., & Chandler, N. (2004). Excavation-induced damage studies at the Underground Research Laboratory. *International Journal of Rock Mechanics and Mining Sciences*, *41*(8), 1413–1426. https://doi.org/10.1016/j.ijrmms.2004.09.010

Meng, Y., Jing, H., Yuan, L. et al. Numerical investigation on the effect of bedding plane properties on mode I fracture characteristics of mudstone with FEM-CZM method. Bull Eng Geol Environ 81, 3 (2022). https://doi.org/10.1007/s10064-021-02515-9

Navidtehrani, Y., Betegon, C., & Martinez-Paneda, E. (2021). A simple and robust Abaqus implementation of the phase field fracture method. Applications in Engineering Science, 6, 100050

Ngoma, M. C., & Kolawole, O. (2026). Mechanistic insights across curing regimes for enzymatic and biopolymer-optimized reinforcement in rock masses. *Deep Underground Science and Engineering*. https://doi.org/10.1002/dug2.70079.

Niu, Q., Jiang, L., Li, C., Zhao, Y., Wang, Q., & Yuan, A. (2023). Application and prospects of 3D printing in physical experiments of rock mass mechanics and engineering: materials, methodologies and models. *International Journal of Coal Science & Technology*, *10*(1). https://doi.org/10.1007/s40789-023-00567-8.

Oppong, F., & Kolawole, O. (2025). Novel nanomagnetic-based slurry for grouting fractured rocks. *Discover Civil Engineering, 2*(1). https://doi.org/10.1007/s44290-024-00157-w

Park, K., & Paulino, G. H. (2013). Cohesive Zone Models: A Critical review of Traction-Separation relationships across fracture surfaces. Applied Mechanics Reviews, 64(6). https://doi.org/10.1115/1.4023110.

Pérez-Rey, I., Muñoz-Ibáñez, A., González-Fernández, M. A., Muñiz-Menéndez, M., Penabad, M. H., Estévez-Ventosa, X., Delgado, J., & Alejano, L. R. (2023). Size effects on the tensile strength and fracture toughness of granitic rock in different tests. *Journal of Rock Mechanics and Geotechnical Engineering*, *15*(9), 2179–2192. https://doi.org/10.1016/j.jrmge.2022.11.005.

Perras, M. A., & Diederichs, M. S. (2014). A review of the tensile strength of Rock: Concepts and testing. *Geotechnical and Geological Engineering*, *32*(2), 525–546. https://doi.org/10.1007/s10706-014-9732-0

Saksala, T., Hokka, M., Kuokkala, V., & Mäkinen, J. (2013). Numerical modeling and experimentation of dynamic Brazilian disc test on Kuru granite. International Journal of Rock Mechanics and Mining Sciences, 59, 128–138. https://doi.org/10.1016/j.ijrmms.2012.12.018

Salimian, M., Baghbanan, A., Hashemolhosseini, H., Dehghanipoodeh, M., & Norouzi, S. (2017). Effect of grouting on shear behavior of rock joint. *International Journal of Rock Mechanics and Mining Sciences*, *98*, 159–166. https://doi.org/10.1016/j.ijrmms.2017.07.002.

Sang, H., Liu, B., Liu, Q., Kang, Y., & Lu, C. (2024). Study of grouting reinforcement mechanism in fractured rock Mass and its engineering application. *International Journal of Geomechanics*, *24*(5). https://doi.org/10.1061/ijgnai.gmeng-9366

Shen, B., & Barton, N. (2018). Rock fracturing mechanisms around underground openings. *Geomech. Eng*, *16*(1), 35-47. https://doi.org/10.12989/gae.2018.16.1.035.

Shojaei, A. K., Shao, J. (2017). Porous Rock Failure Mechanics: Hydraulic Fracturing, Drilling and Structural Engineering. In *Application to Hydraulic Fracturing, Drilling and Structural Engineering* (pp. xv–xviii). https://doi.org/10.1016/b978-0-08-100781-5.00021-x.

Song, Z., Wu, C., Li, Z., Zhang, S., Shen, D., & Zhang, F. (2026). Permeability Reduction of Rough Rock Fracture Through Microbially Induced Carbonate Precipitation. Rock Mechanics and Rock Engineering. https://doi.org/10.1007/s00603-026-05294-5 .

Sonibare M.O., Kolawole O. (2025). Fracture Angularity Influence on Failure Behavior of Grouted Rocks for Geohazard Mitigation. *American Society of Civil Engineers, ASCE Geo-Extreme 2025, Long Beach, California, USA*. https://doi.org/10.1061/9780784486511.013.

Sonibare M.O., Mgiba C., Kolawole O. (2025). Effect of Fracture Orientation on Mechanical Behavior of Grouted Rocks. *American Rock Mechanics Association, 59th U.S. Rock Mechanics/Geomechanics Symposium, Santa Fe, New Mexico, ARMA-2025-0042*.

Sonibare M.O., Mgiba C., Kolawole O. (2026). Influence of Fracture Orientation and Aperture on Grouting Reinforcement of Fractured Surrounding Rock: Experimental and Numerical Study. *Geomechanics for Energy and the Environment*, 46, 100834, 1-12. DOI: 10.1016/j.gete.2026.100834

Stacey, T. (1981). A simple extension strain criterion for fracture of brittle rock. *International Journal of Rock Mechanics and Mining Sciences & Geomechanics Abstracts*, *18*(6), 469–474. https://doi.org/10.1016/0148-9062(81)90511-8

Tang, C. A., Liang, Z. Z., Zhang, Y. B., Chang, X., Tao, X., Wang, D. K., Zhang, J. X., Liu, J. S., Zhu, W. C., & Elsworth, D. (2017). Fracture spacing in layered materials: A new explanation based on two-dimensional failure process modeling. American Journal of Science, 308(1), 49-72.

Terzaghi, K. (1946). Rock defects and loads on tunnel supports, in Proctor, R.V., and White, T.L., eds., Rock tunneling with steel support, Volume 1: Youngstown, Ohio, Commercial Shearing and Stamping Company p. 17-99.

Úcar, R., Belandria, N., Corredor, A., & Arlegui, L. (2023). Planar slope failure in heavily jointed rock: tension cracks and nonlinear strength. *Geotechnical and Geological Engineering*, *42*(2), 1471–1486. https://doi.org/10.1007/s10706-023-02629-9

Wang, C., Li, X., Xiong, Z., Wang, C., Su, C., & Zhang, Y. (2019). Experimental study on the effect of grouting reinforcement on the shear strength of a fractured rock mass. *PLoS ONE*, *14*(8), e0220643. https://doi.org/10.1371/journal.pone.0220643.

Wang, X., Gao, Q., & Li, X. (2022). Layer orientation effect on fracture mode and acoustic emission characteristics of continental shale. *Applied Sciences*, *12*(17), 8683. https://doi.org/10.3390/app12178683

Wang, X., Liu, J., Zhang, G., Li, W., & He, C. (2025). Instability mechanism and failure characteristics of underground cavern in block system under the action of seismic waves. *Deep Underground Science and Engineering*. https://doi.org/10.1002/dug2.70068

Wen, J., Deng, C., Wang, H., Tang, L., & Yu, J. (2025). Critical expansion points: Mechanical signs of surrounding rock instability. *Deep Underground Science and Engineering*. https://doi.org/10.1002/dug2.70049.

Wen, S., Huang, R., Zhang, C., & Zhao, X. (2023). Mechanical behavior and failure mechanism of composite layered rocks under dynamic tensile loading. *International Journal of Rock Mechanics and Mining Sciences*, *170*, 105533. https://doi.org/10.1016/j.ijrmms.2023.105533

Wu, Y. L., Wang, Y. H., & Xu, M. G. (2003). Effect of bolt in jointed rock mass under mixed loading of tension and shearing. *Chinese Journal of Rock Mechanics and Engineering*, *22*(5).

Xu, H., Li, S., Xu, D., Jang, Q., Liu, L., Zheng, M., & Liu, X. (2025). Investigation of parallel joint density thresholds for granite tunnel failure based on physical model experiments and multiscale monitoring techniques. *Scientific Reports*, *15*(1), 28729. https://doi.org/10.1038/s41598-025-13607-x.

Yao, Z., Li, M., Huang, S., Chang, M., & Yang, Z. (2024). Study on the impact of grouting reinforcement on the mechanical behavior of non-penetrating fracture sandstone. *Construction and Building Materials*, *453*, 139079. https://doi.org/10.1016/j.conbuildmat.2024.139079.

Yu, C., & Tian, W. (2024). Application and prospective of sand-type 3D printing material in rock mechanics: a review. *Rapid Prototyping Journal*, *30*(6), 1057–1069. https://doi.org/10.1108/rpj-12-2023-0427

Yuan, S., Sun, Q., Hu, J., Zhang, L., & Geng, J. (2025). Study on the composite fracture characteristics of filling and reinforcing cracked rock mass after high temperature damage. *Deep Underground Science and Engineering*. https://doi.org/10.1002/dug2.70070.

Zafar, S., Hedayat, A., & Moradian, O. (2022). Evolution of tensile and shear cracking in crystalline rocks under compression. *Theoretical and Applied Fracture Mechanics*, *118*, 103254. https://doi.org/10.1016/j.tafmec.2022.103254

Zhang, K., Zhang, K., Zhang, K., Zhang, K., Jin, K., Hu, K., & Xie, J. (2023a). Influence of intermittent opening density on mechanical behavior and fracture characteristics of 3D-printed rock. *Theoretical and Applied Fracture Mechanics*, *124*, 103764. https://doi.org/10.1016/j.tafmec.2023.103764.

Zhang, Z., Jiang, L., Li, C., Zhao, Y., Sainoki, A., & Gong, X. (2023b). Characteristics and mechanism of time on sand powder 3D printing rock analogue: a new method for fractured rock mechanics. *Geomechanics and Geophysics for Geo-Energy and Geo-Resources*, *9*(1). https://doi.org/10.1007/s40948-023-00707-z

Zhou, Changtai, Yichao Rui, Jiadong Qiu, Zhihe Wang, Tao Zhou, Xiting Long, and Ke Shan. (2025). The Role of Fracture in Dynamic Tensile Responses of Fractured Rock Mass: Insight from a Particle-Based Model." International Journal of Coal Science & Technology 12(1):39. https://doi.org/10.1007/s40789-025-00777-2.

Zhou, S., Zhuang, X., Zhou, J., & Liu, F. (2021). Phase field characterization of rock fractures in Brazilian splitting test specimens containing voids and inclusions. International Journal of Geomechanics, 21(3). https://doi.org/10.1061/(asce)gm.1943-5622.0001930

Zhu, G., Zhang, Q., Liu, R., Bai, J., Li, W., & Feng, X. (2021). Experimental and Numerical Study on the Permeation Grouting Diffusion Mechanism considering Filtration Effects. Geofluids, 2021, 1-11. https://doi.org/10.1155/2021/6613990

Zhu, W., & Tang, C. (2006). Numerical simulation of Brazilian disk rock failure under static and dynamic loading. International Journal of Rock Mechanics and Mining Sciences, 43(2), 236–252. https://doi.org/10.1016/j.ijrmms.2005.06.008.